Research Article | Open Access

Catalysis, Energy and Environment

Liu *et al. Catal. Energy Environ.* **2026**, *1*, 9 **DOI:**10.20517/cee.2026.18

Unveiling proton-regulated Mo=O/Mo-O$^-$ centers in reconstructed Ni_2Mo-NiOOH/MoO_x interfaces toward accelerated proton-coupled electron transfer for urea oxidation reaction

Jinshan Liu[1], Miao Zhou[1,2], Chengyi Wang[1,2], Li Zhou[1,2], Mengnan Ruan[1,2,*], Zhifeng Liu[1,2,*]

Keywords:
NiMo alloy, proton-capturing, charge redistribution, proton-coupled electron transfer, urea oxidation reaction

Citation: Liu, J.; Zhou, M.; Wang, C.; Zhou, L.; Ruan, M.; Liu, Z. Unveiling proton-regulated Mo=O/Mo-O$^-$ centers in reconstructed Ni_2Mo-NiOOH/MoO_x interfaces toward accelerated proton-coupled electron transfer for urea oxidation reaction. *Catal. Energy Environ.* **2026**, *1*, 9. https://dx.doi.org/10.20517/cee.2026.18

Received: 11 Aug 2026 **First Decision:** 5 Sep 2026 **Revised:** 8 Oct 2026 **Accepted:** 14 Oct 2026 **Published:** 30 Oct 2026

Academic Editor: Yongfa Zhu **Copy Editor:** Tong Wang **Production Editor:** Tong Wang

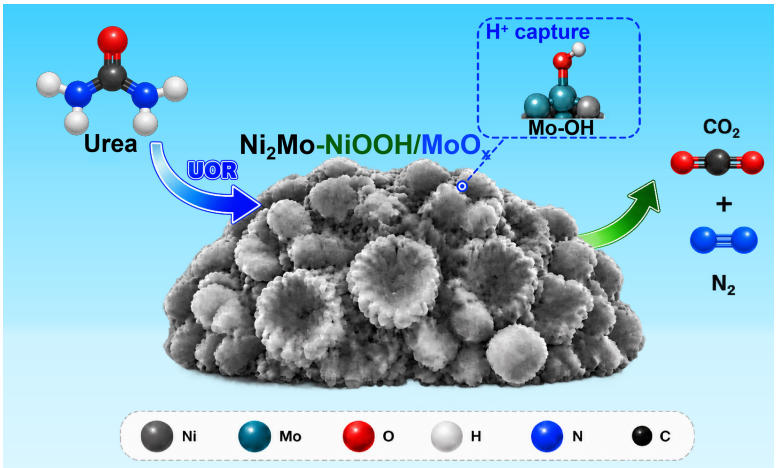

Abstract

Urea electrolysis for hydrogen production offers the dual benefits of low energy consumption and pollutant degradation; however, the sluggish proton-coupled electron transfer (PCET) kinetics remain a critical bottleneck limiting performance enhancement. To overcome this challenge, we herein construct an *in situ* reconstructed NiMo alloy electrocatalyst featuring highly efficient proton-capturing sites to accelerate reaction kinetics. Under anodic conditions, the NiMo alloy undergoes surface reconstruction to form a Ni_2Mo-NiOOH/MoO_x composite structure, where NiOOH functions as the oxidative active site driving the urea oxidation reaction (UOR), while Mo=O/Mo-O$^-$ species in MoO_x act as proton-capturing centers. These sites rapidly sequester protons released during the dehydrogenation of *-NH_2 intermediates, substantially lowering the energy barrier of the key reaction step and facilitating the PCET process. Simultaneously, Mo-induced charge redistribution optimizes the adsorption of reaction intermediates, enabling synergistic modulation of electron and proton transfer. Benefiting from these mechanisms, the

[1]School of Materials Science and Engineering, Tianjin Chengjian University, Tianjin 300384, China.
[2]Tianjin Key Laboratory of Building Green Functional Materials, Tianjin Chengjian University, Tianjin 300384, China.

[*]**Correspondence to:** Prof. Mengnan Ruan, Prof. Zhifeng Liu, School of Materials Science and Engineering, Tianjin Chengjian University, Tianjin 300384, China. E-mail: ruanmengnan@tcu.edu.cn; zhf_liu@tcu.edu.cn

as-fabricated catalyst requires only 1.341 V to achieve a current density of 100 mA·cm^{-2}, exhibiting outstanding reaction kinetics. Moreover, a urea degradation efficiency of 97.21% is attained within 420 min, demonstrating the synergistic enhancement of energy conversion and pollutant removal. This work not only elucidates the pivotal role of PCET modulation in UOR via efficient proton-capturing sites but also provides a new strategy for the rational design of high-performance electrocatalytic systems.

INTRODUCTION

In recent years, driven by the global energy structure transition and the "dual carbon" goals, the development of efficient and sustainable hydrogen production technologies has emerged as a major research focus in the energy field. Among them, water electrolysis for hydrogen production is regarded as one of the key pathways to realizing the hydrogen economy, owing to its inherent advantages of being green, clean, and highly compatible with renewable energy[1-4]. However, conventional water electrolysis systems rely heavily on high-purity freshwater resources, and against the backdrop of growing global water scarcity, this limitation severely hinders their large-scale deployment[5-7]. Therefore, developing alternative anodic reactions to replace the conventional oxygen evolution reaction (OER) is of great significance for reducing energy consumption and expanding the application scenarios of electrolysis systems.

Against this background, the urea oxidation reaction (UOR) has attracted widespread attention due to its unique advantages[8-14]. Conventional water electrolysis consists of the cathodic hydrogen evolution reaction (HER) and the anodic OER, among which OER involves a complex four-electron transfer process with sluggish reaction kinetics, acting as the critical bottleneck limiting the overall energy conversion efficiency[15-22]. In contrast, the theoretical potential of UOR is only 0.37 V, far lower than the 1.23 V of OER, which can significantly reduce the energy consumption of electrolysis[23-26]. Furthermore, urea is widely present in industrial wastewater, agricultural aquaculture wastewater, and municipal domestic sewage. Its electrocatalytic oxidation enables the synergistic realization of hydrogen production and pollutant degradation, thereby constructing an integrated system for energy conversion and environmental remediation[27-30]. From an environmental perspective, untreated urea-containing wastewater is prone to hydrolysis in natural environments, generating ammonia and its derivatives that in turn trigger water eutrophication and ecological pollution issues[31]. In electrocatalytic systems, by contrast, urea can be selectively oxidized to harmless N_2 and CO_2, achieving efficient pollutant removal[32-34]. Meanwhile, this reaction process avoids the safety hazards associated with the mixing of H_2 and O_2 in conventional water electrolysis. Consequently, UOR not only exhibits prominent advantages in energy conversion but also demonstrates significant application potential in environmental governance.

Although UOR exhibits distinct thermodynamic superiority, its reaction pathway involves six-electron transfer[35,36], C-N bond cleavage[37,38] and successive N-H[39,40] dehydrogenation processes. The complicated reaction route leads to sluggish kinetics, making the actual operating potential far higher than the theoretical value[41,42]. Current research mainly concentrates on regulating the adsorption strength of catalysts toward reaction intermediates (e.g., *NH_2, *NH, *NCO) to optimize the reaction pathway and lower the energy barrier[43]. Nevertheless, most of these strategies are merely limited to the modulation of electronic structure, while paying insufficient attention to the critical proton transfer behavior during the reaction. In fact, electron and proton transfer are generally coupled in many electrochemical reaction processes through the proton-coupled electron transfer (PCET) mechanism, which plays an important role in multi-step UOR reactions[44,45]. In particular, the conversion of *-NH_2 to *-NH belongs to a typical dehydrogenation step. Without efficient proton-accepting sites, the released H^+ cannot be transferred timely, which substantially increases the reaction energy barrier and induces intermediate accumulation, thereby restricting the overall reaction rate[39]. Accordingly, starting from the intrinsic reaction nature, constructing catalytic interfaces that can effectively promote proton transfer is a critical route to break the kinetic bottleneck of UOR.

Among diverse catalytic systems, Ni-based materials are recognized as the core active centers for UOR, because they can be *in situ* converted into highly active NiOOH species under alkaline conditions[46]. The high-valent Ni^{3+}/Ni^{4+} species in NiOOH can efficiently accelerate the oxidation process of urea molecules. However, single-component Ni-based systems still have apparent limitations. Their relatively high d-band center endows them with strong adsorption capacity toward reaction intermediates. Although this is beneficial to reaction initiation, it easily causes difficult desorption of intermediates, further leading to active site poisoning and restricted reaction kinetics[47]. To overcome the above shortcomings, researchers have proposed introducing secondary metals via an alloying strategy to regulate the electronic structure of Ni. For instance, NiFe[48] and NiCo[49] systems can optimize intermediate adsorption behavior and improve catalytic performance to a certain degree. Nevertheless, these strategies mainly focus on electronic structure regulation and adsorption optimization, and lack targeted design for the pivotal proton transfer step in UOR. Hence, it is still difficult to fundamentally break through the kinetic limitations of the reaction.

Based on the above background, this work proposes a catalytic design strategy via synergistic regulation of active sites and proton-capturing sites. Under electrochemical conditions, the Ni_2Mo alloy is further *in situ* reconstructed into a Ni_2Mo-NiOOH/MoO_x composite structure, where NiOOH acts as the primary oxidative active site to drive UOR[46,50]. More importantly, the Mo=O/Mo-O^- species in the *in situ* generated MoO_x establish efficient proton-capturing sites, which can rapidly capture the H^+ released during the dehydrogenation of *-NH_2. This significantly reduces the energy barrier of proton transfer and accelerates the key PCET step. This strategy realizes the synergistic modulation of electron and proton transfer, thereby effectively overcoming the bottleneck of restricted dehydrogenation kinetics in conventional catalytic systems. In conclusion, by constructing high-efficiency proton-capturing sites, this study fundamentally resolves the limitation of the critical dehydrogenation step in UOR from the mechanistic perspective, providing a new design insight for the regulation of proton-coupled processes in electrocatalytic reactions.

EXPERIMENTAL

Chemicals and reagents

Nickel sulfate hexahydrate ($NiSO_4·6H_2O$), concentrated hydrochloric acid (HCl), and potassium hydroxide (KOH) were purchased from Tianjin Damao Chemical Reagent Factory with analytical reagent (AR) grade. Sodium molybdate dihydrate ($Na_2MoO_4·2H_2O$) and urea ($CO(NH_2)_2$) were obtained from Tianjin Guangfu Technology Development Co., Ltd. Sodium citrate ($Na_3C_6H_5O_7$) was supplied by Tianjin Aqiluopu Trading Co., Ltd., and anhydrous ethanol (C_2H_6O) was purchased from Tianjin Huihang Chemical Technology Co., Ltd. All the above reagents were used directly without further purification. Nickel foam (NF) with a thickness of approximately 1.5 mm was acquired from Tianjin Anuohe New Energy Technology Co., Ltd. and pretreated before use. In addition, sufficient deionized water was used throughout the entire experimental process.

Preparation of Ni_2Mo/NF

4 mmol $NiSO_4·6H_2O$, 2 mmol $Na_2MoO_4·2H_2O$ and 4.3 mmol $Na_3C_6H_5O_7$ were separately dissolved in 50 mL deionized water, followed by magnetic stirring for 30 min. Afterward, the pH value of the mixed solution was adjusted to 9 using ammonia solution. Electrodeposition was performed at 40 °C for 10 min under a current density of -180 mA·cm^{-2}, with NF as the working electrode, graphite rod as the counter electrode, and saturated calomel electrode (SCE) as the reference electrode. The obtained electrode was rinsed three times with deionized water and then dried in a vacuum drying oven at 60 °C for 6 h. The as-prepared Ni_2Mo/NF catalytic electrode was finally sealed and stored for subsequent use.

Preparation of Ni_2Mo-NiOOH/MoO_x via *in situ* reconstruction

In the electrolyte containing 1 M KOH and 0.33 M urea, *in situ* reconstruction was conducted at a current density of 100 mA·cm^{-2} for 60 min. Ni_2Mo/NF served as the working electrode, graphite rod as the counter electrode, and SCE as the reference electrode. After reconstruction, the sample was ultrasonically treated and dried in an oven to obtain the final product of Ni_2Mo-NiOOH/MoO_x.

Detailed information on material characterizations and electrochemical measurements is provided in the Experimental Section of the Supporting Information.

RESULTS AND DISCUSSION

Morphological and composition analysis

To clarify the correlation between morphological evolution and phase structure of *in situ* reconstructed NiMo-based electrocatalysts, systematic scanning electron microscopy (SEM) and transmission electron microscopy (TEM) characterizations were conducted on the as-prepared catalytic electrodes. As shown in Figure 1A_1 and A_2, the control sample Ni-NiOOH exhibits a uniform nanoparticle array morphology with a compact and flat substrate surface. In comparison, the Ni_2Mo alloy [Figure 1B_1 and B_2] displays a denser particle stacking structure and presents typical alloy substrate features under low-magnification SEM. Further TEM characterization [Supplementary Figure 1] confirms its dense bulk morphology via bright-field TEM observation. The distinct lattice fringes with an interplanar spacing of 0.217 nm in high-resolution transmission electron microscopy (HRTEM) correspond to the (111) crystal plane of Ni_2Mo/NF, demonstrating the successful construction of highly crystalline Ni_2Mo/NF. The polycrystalline ring patterns in selected area electron diffraction (SAED) further validate the crystallinity of the precursor, which provides a fundamental structural basis for the subsequent anodic reconstruction. After anodic *in situ* reconstruction, SEM images of Ni_2Mo-NiOOH/MoO_x [Figure 1C_1 and C_2] show that the original granular morphology disappears and transforms into a rough, defect-enriched reconstructed layer. The inhomogeneous roughening of the substrate surface directly evidences the drastic surface reconstruction during anodic oxidation. Meanwhile, the introduction of Mo induces surface reconstruction and defect exposure, which not only enlarges the electrolyte contact area and increases the density of active sites, but also creates open channels for subsequent proton transfer.

TEM images of Ni_2Mo-NiOOH/MoO_x [Figure 1D] reveal that the overall morphology is well preserved after reconstruction, while a thin and translucent reconstructed shell layer emerges at the edge, which is identified as an amorphous/low-crystalline layer. This indicates that the reconstruction process only occurs on the material surface, and the inner core maintains the Ni_2Mo/NF phase. Such a core-shell structure provides rapid pathways for charge transport. HRTEM images [Figure 1E] clearly identify a triphase heterostructure, including the amorphous MoO_x phase (d = 0.374 nm), crystalline NiOOH active phase (d = 0.209 nm), and Ni_2Mo/NF core (d = 0.217 nm). This result directly confirms the formation of Ni_2Mo-NiOOH/MoO_x heterostructure after *in situ* reconstruction. The intimate contact of the triphase interfaces builds a favorable microenvironment for the synergistic transfer of electrons and protons. The coexistence of crystalline polycrystalline rings and amorphous halos in the SAED pattern [Figure 1F] further verifies the crystalline-amorphous composite structure. Such amorphous features are conducive to enhancing the dynamic surface reconstruction ability and regulating the adsorption behavior of reaction intermediates. Moreover, energy-dispersive X-ray spectroscopy (EDS) elemental mapping [Figure 1G] confirms the coexistence and distribution of Ni, Mo, O and N elements in the reconstructed catalyst. Although the signals of Mo and N are relatively weak due to their low content and surface-related distribution, they can still be detected throughout the material. The presence of Mo indicates the formation of MoO_x during the reconstruction process, while the N signal is mainly attributed to the adsorption of residual urea molecules and N-containing intermediates on the catalyst surface during UOR. This endows abundant Mo=O/Mo-O^-

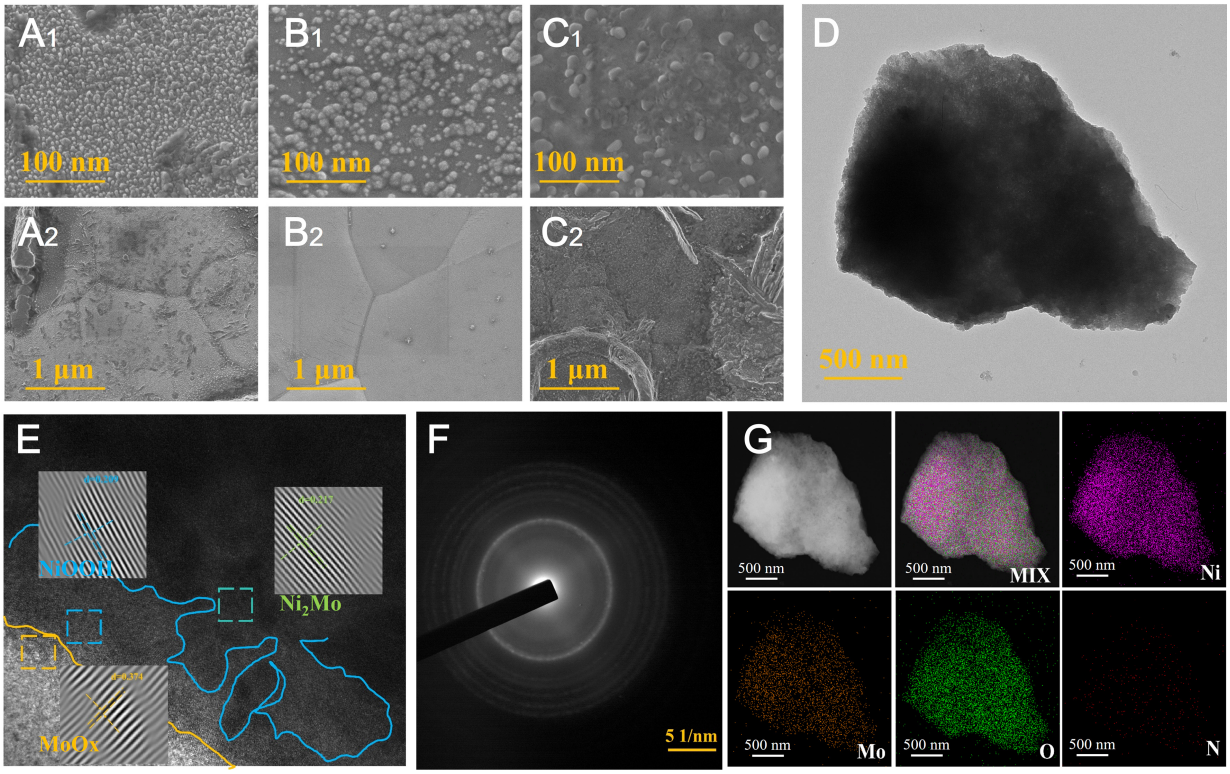

Figure 1. Morphology and structural characterization of the as-prepared catalysts. (A_1 and A_2) SEM images of Ni-NiOOH; (B_1 and B_2) SEM images of Ni_2Mo/NF; (C_1 and C_2) SEM images of Ni_2Mo-NiOOH/MoO_x; (D) TEM image of Ni_2Mo-NiOOH/MoO_x; (E) HRTEM image of Ni_2Mo-NiOOH/MoO_x; (F) SAED pattern of Ni_2Mo-NiOOH/MoO_x; (G) EDS elemental mapping images of Ni_2Mo-NiOOH/MoO_x (Ni, Mo, O, N). SEM: Scanning electron microscopy; NF: nickel foam; HRTEM: high-resolution transmission electron microscopy; EDS: energy-dispersive X-ray spectroscopy; SAED: selected area electron diffraction.

proton-capturing sites for UOR. The above characterization results verify that the *in situ* constructed NiOOH active sites are closely interfaced with MoO_x proton-capturing sites, laying a solid structural foundation for the electrocatalytic reaction.

The phase composition and crystal structure of the samples were systematically analyzed via X-ray diffraction (XRD) [Figure 2A]. The characteristic diffraction peaks of the Ni_2Mo/NF catalytic electrode located at 43.77°, 50.69°, and 73.65° correspond to the (111), (200), and (220) crystal planes, respectively, which are highly consistent with the standard card of NiMo (PDF#03-2714), confirming the successful preparation of Ni_2Mo/NF. The diffraction peaks of the control sample Ni-NiOOH match well with the standard card of β-NiOOH (PDF#06-0141), providing a benchmark for the phase identification of the reconstructed phase. After anodic *in situ* reconstruction, the XRD pattern of Ni_2Mo-NiOOH/MoO_x exhibits obvious phase evolution. The intensity of the characteristic peaks belonging to the Ni_2Mo precursor decreases significantly, indicating that partial reconstruction of the alloy phase occurs during anodic oxidation. Meanwhile, new characteristic peaks emerge at 37.28° and 66.76°, which are assigned to the (002) and (110) crystal planes of β-NiOOH and perfectly match PDF#06-0141. This result verifies the generation of crystalline NiOOH active phases during the reconstruction process. Combined with TEM analysis, the newly formed MoO_x presents an amorphous structure; thus, no crystalline diffraction peaks of MoO_x are detected. Fourier transform infrared spectroscopy (FT-IR) spectroscopy was employed to elucidate the evolution of chemical bonds and functional groups on the catalyst surface [Figure 2B]. Ni_2Mo/NF is dominated by the metallic state with weak signals of metal-oxygen bonds and hydroxyl functional groups. After anodic *in situ* reconstruction, Ni_2Mo-NiOOH/MoO_x shows remarkably enhanced characteristic absorption peaks in the

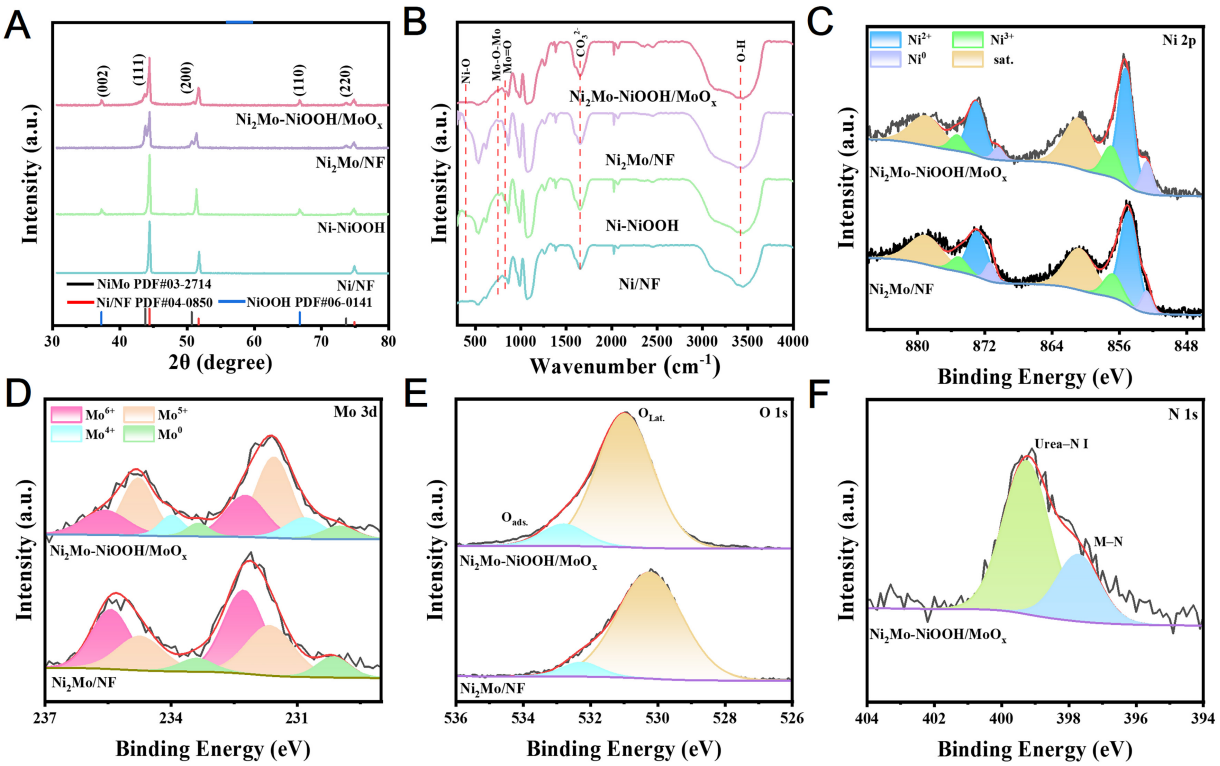

Figure 2. Phase, surface chemical and valence state characterization of catalytic electrodes. (A) XRD patterns of Ni/NF, Ni-NiOOH, Ni_2Mo/NF and Ni_2Mo-NiOOH/MoO_x; (B) FT-IR spectra of the above catalytic electrodes; (C-E) XPS spectra of Ni_2Mo/NF and Ni_2Mo-NiOOH/MoO_x: (C) Ni 2p, (D) Mo 3d, (E) O 1s; (F) N 1s XPS spectrum of Ni_2Mo-NiOOH/MoO_x. XRD: X-ray diffraction; NF: nickel foam; FT-IR: Fourier transform infrared spectroscopy; XPS: X-ray photoelectron spectroscopy.

range of 400-800 cm^{-1}, which are attributed to the Ni-O bonds of NiOOH as well as the Mo-O and Mo=O bonds of MoO_x species. This confirms the successful formation of NiOOH active phases and MoO_x components after reconstruction. Additionally, the stretching vibration intensity of hydroxyl O-H groups at 3,200-3,600 cm^{-1} increases obviously, suggesting abundant enrichment of hydroxyl groups on the catalyst surface. Furthermore, the rich Mo=O/Mo-O^- functional groups in MoO_x can serve as efficient proton-capturing sites. Meanwhile, the hydrogen bond network constructed by surface *OH effectively connects proton transport pathways, accelerating the migration rate of H^+ released from the dehydrogenation of *-NH_2 during urea oxidation and facilitating the PCET process. These results corroborate the rationality of the material structural design from the molecular functional group perspective.

X-ray photoelectron spectroscopy (XPS) characterization was carried out to further investigate the electronic structure, elemental valence distribution and electron transfer behavior of the catalysts before and after *in situ* reconstruction. All binding energies were calibrated with the C 1s characteristic peak at 284.8 eV as the reference [Supplementary Figure 2]. The XPS survey spectra show that Ni_2Mo/NF mainly presents characteristic signals of Ni and Mo, while the response of O element is extremely weak. After anodic *in situ* reconstruction, the signal intensity of O element in Ni_2Mo-NiOOH/MoO_x is enhanced, and the characteristic peaks of Mo remain stable. It is confirmed that Mo species do not leach during the reconstruction process, but undergo synchronous oxidation and anchor on the catalyst surface, forming a composite structure with coexisting NiOOH and MoO_x phases. As shown in Figure 2C, in the Ni 2p spectra, Ni species in Ni_2Mo/NF are dominated by low-activity Ni^{2+}. The proportion of Ni^{3+} in the Ni $2p_{3/2}$ orbital is only 13.34%, and that in the Ni $2p_{1/2}$ orbital is 7.28%. After anodic *in situ* reconstruction, the proportion of Ni^{3+} in Ni_2Mo-NiOOH/MoO_x increases remarkably to 17.76% in Ni $2p_{3/2}$ and 7.98% in Ni $2p_{1/2}$ [Supplementary Table 1]. The

enrichment of high-valent Ni^{3+} species directly confirms the generation of crystalline NiOOH active phases. Meanwhile, the binding energy of the Ni 2p orbital shifts toward a higher value after reconstruction, which originates from the Mo-induced charge rearrangement effect. Mo has higher electronegativity than Ni, and the formation of MoO_x species during reconstruction induces electron transfer from Ni sites toward Mo. This reduces the electron density around Ni atoms, strengthens the constraint of atomic nuclei on electrons, increases the energy required for electron escape, and ultimately results in a positive shift of binding energy. Such electronic structure regulation promotes the stable formation of high-valent Ni^{3+} active sites, providing electronic structural guarantee for efficient UOR. As shown in Figure 2D and Supplementary Table 2, the Mo 3d XPS spectra reveal the coexistence of Mo species with different oxidation states in the Ni_2Mo/NF catalysts. After anodic electrochemical reconstruction, the relative contributions of different Mo oxidation-state components undergo noticeable changes, indicating a redistribution of the surface chemical states of Mo species, accompanied by the evolution of their local coordination environments. The changes in Mo oxidation states reflect the complex surface reconstruction process associated with the formation of MoO_x-related species. Meanwhile, the electron-enriched MoO_x species possess more coordinatively unsaturated sites, particularly Mo=O/Mo-O^- species. These negatively charged oxygen sites can serve as efficient proton-capturing sites, rapidly capturing H^+ released during the dehydrogenation of *-NH_2 intermediates in UOR, thereby accelerating the PCET process, preventing proton accumulation on the catalyst surface, and lowering the energy barrier of the key reaction step. As shown in Figure 2E, the O 1s spectra exhibit two distinguishable oxygen-containing components. The component located at approximately 531.1 eV is associated with oxygen-containing coordination environments, whereas the higher-binding-energy component at approximately 532.9 eV is related to surface-adsorbed oxygen-containing species. These changes indicate the evolution of the surface oxygen chemical environment of the catalyst during electrochemical reconstruction. As presented in Figure 2F, the N 1s spectrum of Ni_2Mo-NiOOH/MoO_x exhibits distinct characteristic signals, which can be attributed to the residual adsorption signals of urea molecules and dehydrogenated *-NH_2 intermediates on the catalytic electrode after *in situ* reconstruction. This confirms the excellent capacity of the catalyst surface for effective adsorption and activation of reaction intermediates, providing direct electronic structural evidence for the UOR reaction pathway. In general, XPS characterization clarifies the regulatory effect of anodic *in situ* reconstruction on the electronic structure of catalysts from the perspectives of elemental valence state, electron density and charge rearrangement mechanisms. On the one hand, the reconstruction process promotes the transformation of Ni species into high-valent Ni^{3+}, and the increase in the proportion of Ni^{3+} directly raises the number of UOR active sites. On the other hand, the Mo-induced charge rearrangement effect remodels the electronic environment of Ni and Mo sites, reducing the electron density of Ni active sites while increasing that of Mo sites. It not only optimizes the adsorption behavior of reaction intermediates, but also provides an electron-enriched structural basis for MoO_x proton-capturing sites. The synergistic optimization of valence state transition and electron cloud distribution not only realizes the synergistic regulation of NiOOH active sites and MoO_x proton-capturing sites, but also elucidates the intrinsic mechanism of Ni_2Mo-NiOOH/MoO_x accelerating UOR reaction kinetics from the electronic perspective. This work provides direct electronic structural evidence for the proposed *in situ* reconstruction synergistic catalytic strategy.

In situ Raman analysis during UOR

To reveal the *in situ* phase evolution and proton-capturing mechanism of the Ni_2Mo-NiOOH/MoO_x catalytic electrode in the UOR, *in situ* Raman spectroscopy was adopted to real-time track the surface structure and species evolution of the catalyst during anodic polarization. Figure 3 compares Ni-NiOOH and Ni_2Mo-NiOOH/MoO_x in terms of spectral features in different wavenumber ranges and three-dimensional *in situ* Raman profiles under UOR conditions. The region of 440-600 cm^{-1} is assigned to the bending and stretching vibration signals of Ni-O bonds in NiOOH. For the Ni-NiOOH catalytic electrode [Figure 3A], obvious characteristic Raman peaks of NiOOH can only be observed at a relatively high anodic polarization potential,

and the peak intensity increases slowly with rising potential. This indicates that without amorphous MoO_x, the *in situ* reconstruction of Ni sites into the high-activity NiOOH phase exhibits a delayed process with a high phase-transition energy barrier, which is unfavorable for the rapid initiation of UOR. In contrast, Ni_2Mo-NiOOH/MoO_x presents distinct NiOOH characteristic signals even at a much lower applied potential [Figure 3D], and the peak intensity grows rapidly as the anodic potential increases. This confirms that the introduction of amorphous MoO_x effectively reduces the energy barrier for *in situ* reconstruction of the active phase. Meanwhile, amorphous MoO_x induces local charge rearrangement, modulates the electronic structure of Ni active centers, and optimizes the adsorption configuration and adsorption strength of UOR intermediates. Characteristic signals associated with MoO_x-related species can be further identified in the high wavenumber range of 980-1,020 cm^{-1}. Combined with the two-dimensional stacked *in situ* Raman spectra [Supplementary Figure 3], the Ni-NiOOH system shows no obvious characteristic response in this wavenumber region throughout the test [Supplementary Figure 3A]. By comparison, the Ni_2Mo-NiOOH/MoO_x sample [Supplementary Figure 3B] displays well-resolved characteristic Raman peaks that gradually strengthen with increasing potential. These signals are attributed to the stretching vibrations of terminal Mo=O double bonds and coordinatively unsaturated Mo-O^- species in the MoO_x phase, which directly proves that the anodic UOR environment can induce the *in situ* generation of MoO_x active components rich in Mo=O/Mo-O^- on the catalyst surface. Moreover, the characteristic peaks of carbonate intermediates derived from UOR evolve synchronously within 1,040-1,100 cm^{-1} [Figure 3C and Figure 3F]. Comparative results demonstrate that Ni_2Mo-NiOOH/MoO_x possesses a lower onset potential and a more prominent signal response for intermediate peaks. It indicates that Mo=O/Mo-O^- sites can rapidly capture H^+ released from the dehydrogenation of *-NH_2 during urea oxidation, timely alleviate interfacial proton accumulation, markedly lower the energy barrier of the key PCET step, and accelerate the dehydrogenation and intermediate transformation kinetics of UOR. The three-dimensional *in situ* Raman spectra in Figure 3B and Figure 3E further verify that the NiOOH active phase signals, MoO_x characteristic peaks at 980-1,020 cm^{-1}, and high-wavenumber intermediate peaks of the Ni_2Mo-NiOOH/MoO_x system follow synchronous potential-dependent evolution, with highly consistent onset polarization potentials. This confirms that MoO_x species are not inert substrates but synergistically participate in the UOR catalytic process together with NiOOH active sites. To distinguish the behavioral differences between UOR and OER and exclude the interference of structural evolution, *in situ* Raman tests of Ni_2Mo-NiOOH/MoO_x were conducted under OER conditions [Supplementary Figure 4]. The results show that only characteristic vibration signals of NiOOH can be detected during OER, while no obvious Mo=O/Mo-O^- characteristic response appears in the 980-1,020 cm^{-1} region. This fully verifies that the MoO_x characteristic signals in this wavenumber range are specifically triggered by the dehydrogenation and proton-releasing process of *-NH_2 in UOR, which directly corresponds to proton-capturing behavior rather than simple potential-induced phase transition.

In summary, the *in situ* Raman results confirm that a Ni_2Mo-NiOOH/MoO_x composite active interface is *in situ* constructed on Ni_2Mo/NF under anodic UOR conditions. In this system, NiOOH acts as the core oxidative active site to drive urea molecule adsorption and bond dissociation, while Mo=O/Mo-O^- species in MoO_x characterized at 980-1,020 cm^{-1} serve as efficient proton-capturing sites. These sites rapidly anchor and transfer protons released from *-NH_2 dehydrogenation, relieve interfacial proton accumulation, and accelerate the PCET process. Meanwhile, Mo-induced electronic rearrangement finely regulates the adsorption behavior of reaction intermediates and realizes the synergistic coupling of electron transfer and proton transport. Collectively, these effects enhance the UOR catalytic performance of the catalyst from both structural and kinetic perspectives.

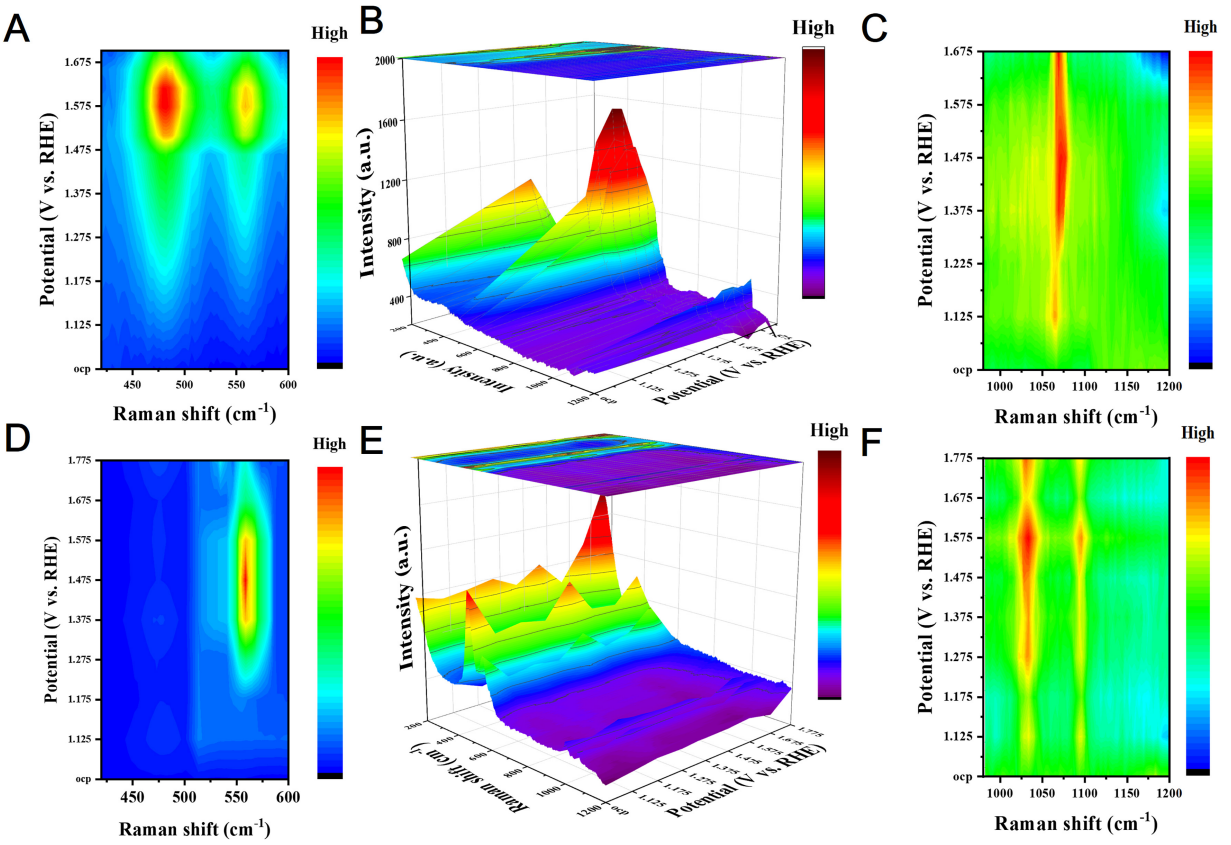

Figure 3. Operando Raman spectra of catalytic electrodes under UOR. (A-C) Operando Raman spectra of Ni-NiOOH at varied anodic potentials: (A) 2D contour plot in the range of 440-600 cm^{-1}; (B) corresponding 3D waterfall plot; (C) 2D contour plot in the range of 980-1,200 cm^{-1}; (D-F) Operando Raman spectra of Ni_2Mo-NiOOH/MoO_x at varied anodic potentials: (D) 2D contour plot in the range of 440-600 cm^{-1}; (E) corresponding 3D waterfall plot; (F) 2D contour plot in the range of 980-1,200 cm^{-1}. RHE: Reversible hydrogen electrode; UOR: urea oxidation reaction.

Electrochemical performance analysis for UOR

Electrochemical measurements were performed to verify the synergistic effect between the *in situ* reconstructed Ni_2Mo-NiOOH/MoO_x catalytic electrode and MoO_x proton-capturing sites from the perspectives of catalytic activity, reaction kinetics and reaction selectivity. A standard three-electrode configuration was adopted throughout the electrochemical tests. The UOR performance of the catalysts was evaluated in 1.0 M KOH solution containing 0.33 M urea, while the OER performance was measured in pure 1.0 M KOH electrolyte. Optimization experiments on the Ni/Mo precursor molar ratio [Supplementary Figure 5A] and *in situ* reconstruction duration of Ni_2Mo/NF [Supplementary Figure 5B] were systematically conducted. The results demonstrate that Ni_2Mo/NF with a Ni/Mo ratio of 2 exhibits the optimal UOR activity. This can be attributed to the balanced synergy between NiOOH active sites and MoO_x proton-capturing sites. An insufficient Mo content leads to the formation of fewer MoO_x species and limited proton-capturing capability, whereas excessive Mo incorporation reduces the proportion of NiOOH active sites, resulting in an unfavorable catalytic balance. Moreover, the Ni_2Mo-NiOOH/MoO_x electrode obtained after 60 min of *in situ* reconstruction delivers the best UOR performance, providing the basis for subsequent electrochemical studies.

The linear sweep voltammetry (LSV) curves in Figure 4A compare the current density of bare Ni/NF, Ni-NiOOH, Ni_2Mo/NF and *in situ* reconstructed Ni_2Mo-NiOOH/MoO_x at the same applied potential. It is clearly observed that Ni_2Mo-NiOOH/MoO_x with MoO_x proton-capturing sites induced by anodic reconstruction exhibits remarkably superior UOR performance to other control catalysts. It should be noted

that the potential differences presented in the inset of Figure 4A were calculated by subtracting the theoretical equilibrium potential of OER [1.23 V *vs.* reversible hydrogen electrode (RHE)] from the measured UOR operating potentials. Here, the OER equilibrium potential is employed solely as a common reference benchmark to facilitate a comparative evaluation of the operating potentials required by different catalysts. The as-prepared Ni_2Mo-NiOOH/MoO_x exhibits outstanding UOR activity, requiring only 1.341 and 1.352 V *vs.* RHE to reach current densities of 100 and 200 mA·cm^{-2}, respectively, corresponding to only 111 and 122 mV higher potentials than the theoretical OER potential (1.23 V). These values are far lower than those of Ni_2Mo/NF (125 mV, 151 mV), Ni-NiOOH (183 mV, 252 mV) and Ni/NF (213 mV, 313 mV). Meanwhile, Ni_2Mo-NiOOH/MoO_x also shows better OER performance than other counterparts [Supplementary Figure 6A]. The enhanced current density at the same potential originates from the spontaneous reconstruction of Ni_2Mo/NF into high-activity NiOOH phases under anodic conditions, which provides abundant oxidative active sites for UOR. Meanwhile, the generated MoO_x is rich in Mo=O/Mo-O$^-$species, which act as efficient proton-capturing sites to rapidly trap H^+ released during the dehydrogenation of *-NH_2 and alleviate interfacial proton accumulation. Furthermore, Mo-induced charge rearrangement further optimizes the adsorption-desorption behavior of UOR intermediates. The synergistic effect of the above two aspects greatly improves the catalytic activity and charge transport efficiency. Tafel slope analysis based on Figure 4B shows that Ni_2Mo-NiOOH/MoO_x possesses the smallest Tafel slope of 32.36 mV·dec^{-1}, which is markedly lower than those of Ni_2Mo/NF (64.76 mV·dec^{-1}), Ni-NiOOH (143.06 mV·dec^{-1}) and Ni/NF (166.72 mV·dec^{-1}). The Tafel slope directly reflects the energy barrier of the rate-determining step (RDS). This result confirms that the synergistic cooperation between NiOOH active sites and MoO_x proton-capturing sites effectively reduces the energy barrier of the PCET step during UOR. The proton-capturing effect of MoO_x species accelerates the rapid diversion of interfacial protons and avoids kinetic hysteresis caused by proton accumulation. In addition, Mo-induced local charge rearrangement optimizes the charge transport pathway and intermediate transformation process, thereby remarkably accelerating the reaction rate and achieving superior reaction kinetics. To further verify the product selectivity of the UOR process, the generated N_2 product was quantitatively analyzed, and the corresponding Faradaic efficiency (FE) was calculated. As shown in Supplementary Figure 6B, the amount of N_2 continuously increases with electrolysis time, exhibiting an approximately linear growth trend, which indicates the stable conversion of urea during the electrochemical oxidation process. Moreover, the FE for N_2 production remains at a high level of approximately 93%-95% throughout the electrolysis period, demonstrating the high selectivity of Ni_2Mo-NiOOH/MoO_x toward nitrogen conversion.

Electrochemical impedance spectroscopy (EIS), phase angle analysis, cyclic voltammetry (CV) and double-layer capacitance (C_{dl}) measurements were performed to clarify the synergistic enhancement mechanism of the *in situ* reconstructed Ni_2Mo-NiOOH/MoO_x composite structure and MoO_x proton-capturing sites toward UOR performance from the aspects of charge transport efficiency, active site exposure and intrinsic reaction kinetics.

In terms of charge transport, the Nyquist plots presented in Figure 4C and Supplementary Table 3 show the impedance values of Ni_2Mo-NiOOH/MoO_x, Ni_2Mo/NF, Ni-NiOOH and Ni/NF measured at an open-circuit potential of 0.23 V are 5.81, 10.43, 16.45 and 19.64 Ω, respectively. Among all samples, Ni_2Mo-NiOOH/MoO_x exhibits the smallest charge transfer resistance (R_{ct}), implying the lowest charge transfer barrier at the electrode/electrolyte interface. This favorable characteristic originates from the local charge rearrangement induced by Mo during *in situ* reconstruction, which optimizes the electron conduction pathway of the composite architecture and reduces the intrinsic electron transport resistance. Meanwhile, the MoO_x proton-capturing sites generated during UOR can rapidly guide interfacial proton migration and avoid interfacial polarization caused by proton accumulation from the dehydrogenation of *-NH_2, thereby greatly improving the charge transfer efficiency. Compared with the Nyquist plots under OER conditions

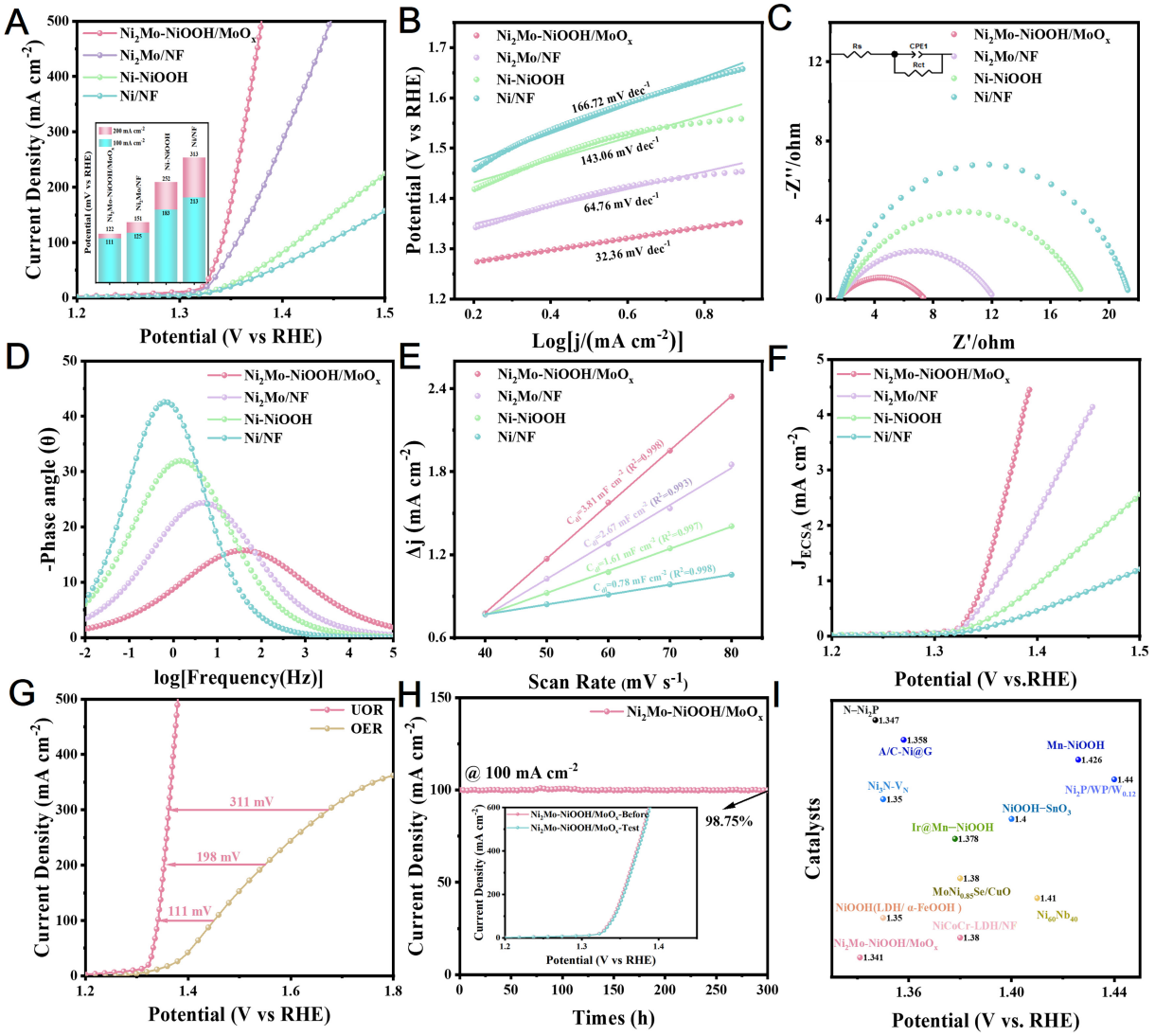

Figure 4. Electrocatalytic UOR performance characterization of various catalysts. (A) LSV curves of Ni_2Mo-NiOOH/MoO_x, Ni_2Mo/NF, Ni-NiOOH and Ni/NF (Inset: Comparison of potential differences relative to the OER equilibrium potential for different catalysts at specific current densities); (B) Corresponding Tafel slope curves (R^2 values above 0.95); (C) Nyquist impedance plots and equivalent circuit model; (D) Bode phase plots; (E) C_{dl} plots (R^2 values above 0.99); (F) ECSA-normalized LSV curves; (G) LSV curve comparison between UOR and OER of Ni_2Mo-NiOOH/MoO_x; (H) 300 h i-t test of Ni_2Mo-NiOOH/MoO_x at the current density of 100 mA·cm^{-2}, with the LSV curves before and after the stability test shown in the inset; (I) Comparison of the potential of Ni_2Mo-NiOOH/MoO_x and other UOR catalysts at a current density of 100 mA·cm^{-2}. NF: Nickel foam; LSV: linear sweep voltammetry; UOR: urea oxidation reaction; OER: oxygen evolution reaction; ECSA: electrochemically active surface area; C_{dl}: double-layer capacitance.

[Supplementary Figure 7A], although Ni_2Mo-NiOOH/MoO_x still delivers a relatively low impedance value, its overall R_{ct} is remarkably higher than that under UOR, and the performance gap with other samples is narrowed. This demonstrates that its low-resistance interfacial property is a specific optimization targeted at the UOR process, rather than a general enhancement of electron conduction. The Bode phase angle plots [Figure 4D and Supplementary Figure 7B] further confirm that the phase angle peak of Ni_2Mo-NiOOH/MoO_x under UOR appears at a higher frequency region with a broader peak shape. This indicates faster high-frequency charge transfer and a stronger coupling effect between the low-frequency electric double layer and Faradaic reaction, which directly reflects that

MoO_x proton-capturing sites accelerate interfacial proton delivery and realize efficient coupling of charge and proton transfer. In contrast, the position difference of phase angle peaks among various samples under OER is negligible, failing to embody the superiority of this synergistic effect.

CV curves recorded at various scan rates under UOR conditions [Supplementary Figure 8] show that Ni_2Mo-NiOOH/MoO_x possesses a much larger enclosed CV area than all control samples, indicative of a higher double-layer capacitance and enhanced electrochemically active surface area (ECSA). Under OER conditions [Supplementary Figure 9], although Ni_2Mo-NiOOH/MoO_x still exhibits a larger CV area, the overall enhancement degree is far lower than that under UOR, further demonstrating that its active sites are more sufficiently utilized during the UOR process. The C_{dl} values calculated from CV curves [Figure 4E, Supplementary Figure 10 and Supplementary Table 4] reveal that Ni_2Mo-NiOOH/MoO_x delivers a markedly higher C_{dl} than Ni_2Mo/NF, Ni-NiOOH and Ni/NF. Given the positive linear correlation between C_{dl} and ECSA, a larger electrochemically active surface area is confirmed for Ni_2Mo-NiOOH/MoO_x. This superiority originates from the structural optimization induced by *in situ* reconstruction. During the transformation of Ni_2Mo/NF into the Ni_2Mo-NiOOH/MoO_x composite structure, abundant active crystal facets and reaction sites are formed on the surface. Meanwhile, the introduction of Mo=O/Mo-O^- optimizes the surface hydrophilicity of the electrode, facilitates electrolyte infiltration, and further improves the accessibility of active sites, providing sufficient reaction interfaces for UOR. As displayed in the ECSA-normalized LSV curves [Figure 4F], Ni_2Mo-NiOOH/MoO_x achieves a higher current density per unit electrochemically active area than other samples. This result indicates that the excellent UOR performance is not merely attributed to the increased number of active sites, but essentially stems from the substantially enhanced intrinsic catalytic activity of individual active sites. The improvement of intrinsic activity strongly verifies the synergistic regulation mechanism between NiOOH active sites and MoO_x proton-capturing sites. NiOOH serves as the core oxidative site to drive the adsorption and bond dissociation of urea molecules, while Mo=O/Mo-O^- species rapidly capture the released H^+ during dehydrogenation, alleviate interfacial proton accumulation, and lower the energy barrier of the PCET step. Moreover, Mo-induced local charge rearrangement modulates the electronic structure of Ni active centers and regulates the adsorption-desorption behavior of UOR intermediates, thereby remarkably boosting the reaction rate of individual active sites.

Figure 4G shows the LSV comparison between UOR and OER, which further reflects the specific performance advantages of the catalyst. At the same current density, Ni_2Mo-NiOOH/MoO_x exhibits remarkably higher activity in UOR than in OER, accompanied by a much lower overpotential. This superiority stems from the specific adaptation of MoO_x proton-capturing sites toward the UOR reaction. The Mo=O/Mo-O^- species in MoO_x can only accelerate the PCET process by capturing H^+ released from the *-NH_2 dehydrogenation step during UOR, while they fail to exert the proton-capturing effect in OER lacking rapid proton release. This endows the catalyst with distinctive kinetic advantages toward UOR and achieves energy consumption reduction. A performance radar chart was adopted for comprehensive evaluation across multiple key indicators [Supplementary Figure 11], including Tafel slope, R_{ct}, low overpotential $1/E_{100}$, as well as C_{dl} and ECSA closely related to active site density. The results reveal that Ni_2Mo-NiOOH/MoO_x delivers prominent superiority in all these parameters. A smaller Tafel slope represents favorable reaction kinetics to efficiently drive urea oxidation; a lower R_{ct} indicates ultrahigh charge transport efficiency and reduced energy loss; a higher $1/E_{100}$ corresponds to a lower overpotential at 100 $mA \cdot cm^{-2}$, reflecting outstanding energy-saving effect and lowering the energy input required for the reaction. Larger C_{dl} and ECSA values demonstrate abundant active sites on the electrode surface, providing sufficient catalytic interfaces for the reaction. These merits jointly construct an all-round optimized performance matrix, which strongly verifies that the synergistic cooperation between NiOOH active sites and MoO_x proton-capturing sites in the *in situ* reconstructed Ni_2Mo-NiOOH/MoO_x composite structure realizes the full-scale optimization of electrocatalytic performance.

Figure 4H presents the i-t curve of Ni_2Mo-NiOOH/MoO_x for continuous steady-state operation over 300 h at 100 mA·cm^{-2}. The current density maintains stable output without obvious attenuation throughout the ultra-long cycling period. Among them, the inset shows the LSV curves before and after the stability test, which almost completely overlap, and no obvious shift of catalytic overpotential is observed, fully demonstrating the excellent electrochemical durability of the catalyst. Such long-term stability benefits from the synergistic superiority of the *in situ* constructed Ni_2Mo-NiOOH/MoO_x composite structure. Thermodynamically stable NiOOH serves as the core oxidative active framework, which effectively inhibits the dissolution loss and excessive oxidation of active components under high anodic potential. Meanwhile, the Mo=O/Mo-O$^-$ species in MoO_x can continuously capture H^+ released from *-NH_2 dehydrogenation during UOR via reversible proton adsorption-desorption cycles, timely relieve interfacial proton accumulation and weaken local polarization corrosion, thus achieving dynamic self-maintenance of proton-capturing sites. Microscopic characterizations were performed on Ni_2Mo-NiOOH/MoO_x after 300 h continuous operation. SEM images [Supplementary Figure 12] confirm that the original microscopic morphology is well preserved without particle aggregation, structural collapse or exfoliation of active phases. Elemental mapping verifies the homogeneous distribution of Ni, Mo and O elements on the material surface. Further TEM characterization [Supplementary Figure 13] confirms at the microscopic scale that the catalyst retains an intact lattice structure without phase separation or structural collapse, and Ni, Mo and O elements still maintain a highly uniform distribution, proving the long-term stability of the heterogeneous interface constructed by NiOOH and MoO_x. Multi-current step V-t test results [Supplementary Figure 14] show that Ni_2Mo-NiOOH/MoO_x can rapidly reach potential equilibrium at each current gradient within a wide current density range of 100-400 mA·cm^{-2}, without obvious potential drift or aggravated polarization. Even under harsh working conditions at high current densities, NiOOH active sites and MoO_x proton-capturing sites still maintain efficient synergistic coupling. By virtue of Mo-induced charge rearrangement to optimize the electron transport pathway and relying on MoO_x to rapidly dissipate enriched protons, the electrode interface always maintains an efficient and stable charge transfer environment under wide-load working conditions. The microscopic characterizations after long-term reaction confirm the intrinsic origin of catalytic stability from the structural perspective. Furthermore, as shown in Figure 4I and Supplementary Table 5, comparison with other modified materials confirms that Ni_2Mo-NiOOH/MoO_x delivers a particularly remarkable performance enhancement.

Ion dependence analysis

To directly verify the pivotal role of Mo=O/Mo-O$^-$ species in the *in situ* reconstructed MoO_x as proton-capturing sites, control experiments were conducted by introducing extra MoO_4^{2-} and Ni^{2+} into the electrolyte, and the relevant results are displayed in Figure 5. In the MoO_4^{2-} addition experiment, the LSV curves of the Ni_2Mo-NiOOH/MoO_x catalyst only show a negligible response with the increase of MoO_4^{2-} concentration [Figure 5A], and the curves almost overlap with those obtained in the original electrolyte, presenting an obvious saturation effect. This is because abundant highly active Mo=O/Mo-O$^-$ proton-capturing sites have been *in situ* generated on the electrode surface during anodic reconstruction. These sites are uniformly distributed on the surface of the NiOOH active phase, which can efficiently trap H^+ released from *-NH_2 dehydrogenation during UOR, alleviate interfacial proton accumulation, and lower the energy barrier of the key PCET step. Therefore, the extra introduced solution-phase MoO_4^{2-} cannot form more effective proton-capturing sites on the pre-reconstructed electrode surface, resulting in a greatly limited performance improvement space. This directly confirms that the UOR performance of the catalyst mainly originates from the *in situ* generated MoO_x proton-capturing sites rather than free Mo species in the solution. In sharp contrast, the control catalytic electrodes including Ni_2Mo/NF, Ni-NiOOH and Ni/NF exhibit an obvious response effect, where the LSV curves shift toward the left and the current density increases remarkably with the rising MoO_4^{2-} concentration [Figure 5B-D]. This phenomenon arises from the lack of intrinsic MoO_x proton-capturing sites on the surface of these catalysts. The dissolved MoO_4^{2-} in the

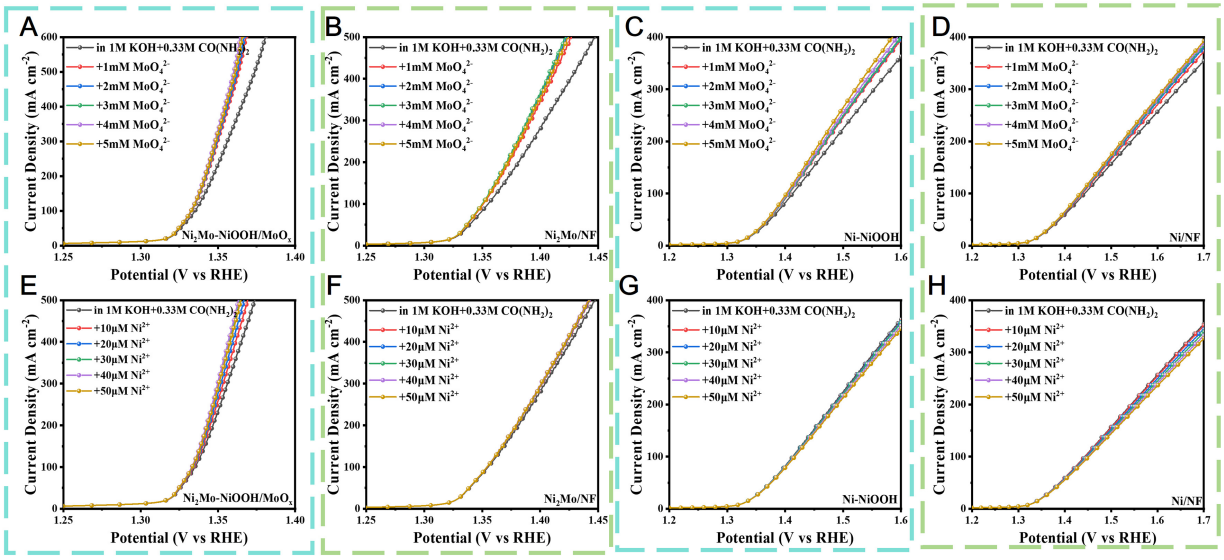

Figure 5. Effects of different concentrations of MoO_4^{2-} and Ni^{2+} in the electrolyte on the UOR electrocatalytic performance of various catalytic electrodes. (A-D) LSV curves of Ni_2Mo-NiOOH/MoO_x, Ni_2Mo/NF, Ni-NiOOH and Ni/NF catalytic electrodes with 0-5 mM MoO_4^{2-} added into the electrolyte containing 1 M KOH and 0.33 M $CO(NH_2)_2$; (E-H) LSV curves of the above catalytic electrodes with 0-50 μM Ni^{2+} added into the electrolyte. RHE: Reversible hydrogen electrode; KOH: potassium hydroxide; LSV: linear sweep voltammetry; UOR: urea oxidation reaction.

solution can be *in situ* converted into Mo=O/Mo-O^- contained MoO_x species on the electrode surface under anodic potential, providing additional proton-capturing capacity for UOR, accelerating PCET kinetics, and thereby substantially reducing the overpotential and boosting catalytic activity. This result indirectly corroborates the essential function of Mo=O/Mo-O^- as proton-capturing sites, and also demonstrates that the MoO_x sites derived from *in situ* reconstruction possess higher stability and efficiency than those formed by Mo species introduced from the bulk solution. In the Ni^{2+} addition tests [Figure 5E-H], the LSV curves of all catalysts remain nearly unchanged and their performance is barely affected by the variation of Ni ion concentration in the electrolyte. This excludes the interference of solution-phase Ni species on UOR activity and further confirms that the performance modulation is specifically attributed to the efficient proton-capturing behavior of Mo=O/Mo-O^- species in MoO_x. Such species can synergize with NiOOH active sites to realize the synergistic regulation of electron and proton transfer during UOR, thereby remarkably accelerating the reaction kinetics.

Electrolyte concentration-dependent kinetic analysis

To intrinsically reveal the modulation mechanism of Mo=O/Mo-O^- proton-capturing sites in MoO_x on UOR reaction kinetics, electrolyte concentration-dependent kinetic tests and redox charge capacity characterization were performed[51]. Direct experimental evidence for the synergistic catalytic mechanism was provided from three aspects, including reaction order, interfacial proton transfer efficiency, and active site utilization efficiency.

In the electrolyte concentration-dependent experiments [Figure 6], the RDS of UOR corresponds to the dehydrogenation of urea molecules. The H^+ released in this process will accumulate at the electrode interface if not removed timely, inhibiting the forward progression of the reaction and inducing kinetic hysteresis. As shown in Figure 6A and C, the LSV curves of Ni_2Mo-NiOOH/MoO_x and Ni_2Mo/NF were obtained at different urea concentrations. The half-wave current density ($j_{1/2}$) exhibits a significant linear positive correlation with urea concentration, yielding a higher slope of 616.64 for Ni_2Mo-NiOOH/MoO_x [Figure 6B], which is much higher than the value of 280.48 for Ni_2Mo/NF [Figure 6D]. The stronger concentration dependence indicates that Ni_2Mo-NiOOH/MoO_x presents

a more sensitive response to urea concentration and a remarkably enhanced urea conversion efficiency. The fundamental origin lies in the fact that the *in situ* generated Mo=O/Mo-O^- species can rapidly trap H^+ released during dehydrogenation, effectively alleviate interfacial proton accumulation, and drive the forward progression of the PCET process. Accordingly, more urea molecules can be efficiently converted with the increase of urea concentration, and the increment of reaction rate is far larger than that of the precursor catalyst without efficient proton-capturing sites. Kinetic tests targeting KOH concentration further confirm the superiority of MoO_x proton-capturing sites. OH^- in the solution acts as both the reactant of UOR and the final proton acceptor. As shown in Figure 6E and G, the LSV curves of Ni_2Mo-NiOOH/MoO_x and Ni_2Mo/NF were obtained at different KOH concentrations. The slope calculated from the Log[j] *vs.* Log[KOH] fitting for Ni_2Mo-NiOOH/MoO_x is 0.546 [Figure 6F], slightly lower than 0.581 for Ni_2Mo/NF [Figure 6H], indicating that this catalyst has a weaker dependence on the OH^- concentration in the electrolyte. This difference originates from the reversible proton capture cycle of Mo=O/Mo-O^-. Mo=O can *in situ* capture H^+ to form Mo-OH, and subsequently regenerate Mo=O by rapidly reacting with OH^-, thus constructing a closed loop of "capture-transfer-regeneration". Efficient proton conduction can be maintained even at low OH^- concentrations. In contrast, Ni_2Mo/NF lacks such surface proton-capturing sites and has to completely depend on OH^- in the solution to accept H^+, rendering it more sensitive to the variation of OH^- concentration and a higher reaction order. Redox charge capacity characterization [Supplementary Figure 15] further verifies the Mo-induced synergistic enhancement effect. The integrated charge (Q) calculated from the LSV curve of Ni_2Mo-NiOOH/MoO_x reaches up to 7,335.64 mC [Supplementary Figure 15A], nearly twice that of Ni_2Mo/NF (3,735.64 mC) [Supplementary Figure 15B], and far higher than those of Ni-NiOOH (2,735.64 mC) [Supplementary Figure 15C] and Ni/NF (1,601.64 mC) [Supplementary Figure 15D]. Such a remarkable difference stems from the dual regulatory effect of Mo. On the one hand, Mo-induced local charge rearrangement during *in situ* reconstruction optimizes the electronic structure of Ni sites, reduces the oxidation potential for the transformation from Ni^{2+} to Ni^{3+}/Ni^{4+}, facilitates the formation of high-activity NiOOH phase, and increases the number of active sites participating in UOR. On the other hand, the proton-capturing effect of MoO_x effectively relieves interfacial proton accumulation and local polarization, avoids the excessive oxidation or dissolution of Ni active sites at high potentials, and substantially improves the utilization efficiency of active sites. Meanwhile, the higher Q value also reflects the reversible redox contribution of Mo sites during proton capture. Mo=O/Mo-O^- undergoes reversible valence state variation in the process of capturing and transferring H^+, further increasing the overall charge transfer capacity. This represents a unique synergistic effect that cannot be achieved by MoO_x-free catalytic electrodes.

In summary, electrolyte concentration-dependent kinetic measurements and redox charge capacity characterization validate the core role of MoO_x proton-capturing sites in Ni_2Mo-NiOOH/MoO_x. By rapidly trapping H^+ released in the dehydrogenation step of UOR, these sites alleviate interfacial proton accumulation and lower the energy barrier of the PCET step. Meanwhile, they optimize the electronic structure and utilization efficiency of Ni active sites, realizing the synergistic regulation of electron and proton transfer. This work provides solid experimental support for its superior UOR kinetic performance.

In situ electrochemical analysis

To reveal the dynamic evolutionary kinetics of interfacial charge transfer and proton transport at the electrode interface during UOR, *in situ* electrochemical EIS measurements were conducted at different potentials. Three-dimensional waterfall plots of Nyquist impedance spectra and Bode phase diagrams were utilized to real-time track the potential-dependent evolution of interfacial reaction behavior, providing *in situ* kinetic evidence for the regulatory effect of MoO_x proton-capturing sites.

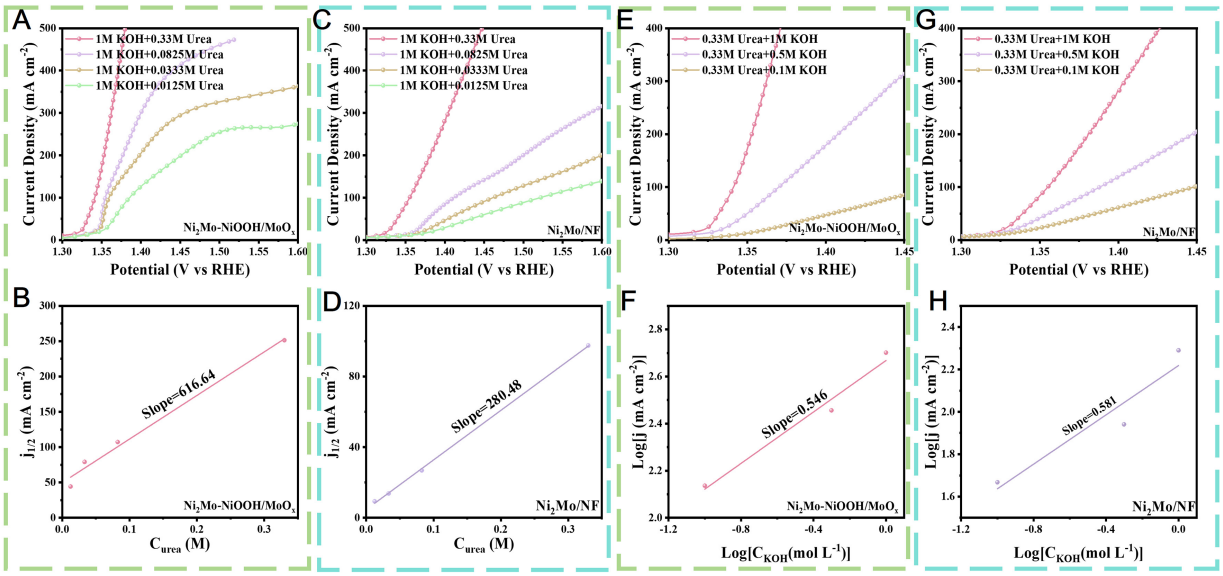

Figure 6. Concentration-dependent kinetic analysis of Ni_2Mo-$NiOOH/MoO_x$ and Ni_2Mo/NF catalysts. (A and C) LSV curves of Ni_2Mo-$NiOOH/MoO_x$ and Ni_2Mo/NF at different urea concentrations (0.0125-0.33 M); (B and D) Linear fitting relationships between $j_{1/2}$ and urea concentration for Ni_2Mo-$NiOOH/MoO_x$ and Ni_2Mo/NF, respectively, reflecting the concentration dependence toward urea oxidation; (E and G) LSV curves of Ni_2Mo-$NiOOH/MoO_x$ and Ni_2Mo/NF at different KOH concentrations (0.1-1 M); (F and H) Log(j)-Log[KOH] fitting curves for Ni_2Mo-$NiOOH/MoO_x$ and Ni_2Mo/NF, respectively, used to determine the apparent reaction order with respect to OH^- concentration. RHE: Reversible hydrogen electrode; NF: nickel foam; KOH: potassium hydroxide; LSV: linear sweep voltammetry; $j_{1/2}$: half-wave current density.

As presented in Figure 7A, the R_{ct} of Ni_2Mo-$NiOOH/MoO_x$ decreases remarkably with the increase of potential and shows an obvious decline even in the low-potential region, reaching the minimum value among all catalysts at 0.65 V. This phenomenon directly confirms the crucial role of *in situ* generated MoO_x species. During UOR, the dehydrogenation of urea-derived *-NH_2 intermediates releases a large quantity of H^+. If these protons cannot be removed promptly, they will accumulate at the electrode interface, induce interfacial polarization, and substantially increase the R_{ct}. In contrast, the Mo=O/Mo-O^- species on the surface of Ni_2Mo-$NiOOH/MoO_x$ can rapidly capture H^+ released from the dehydrogenation process, construct interfacial proton transfer pathways, and effectively alleviate interfacial proton accumulation and polarization effects. Consequently, the R_{ct} is greatly reduced, establishing a low-resistance interfacial environment for the PCET process. In comparison, the R_{ct} of Ni_2Mo/NF [Figure 7B] varies slowly in the low-potential range and remains distinctly higher than that of Ni_2Mo-$NiOOH/MoO_x$, indicating that stable and efficient MoO_x proton-capturing sites are not formed and the capacity of interfacial proton conduction is insufficient. Furthermore, the R_{ct} variation of the Ni-NiOOH catalyst [Figure 7C] exhibits a more delayed trend, with only a limited decline at high potentials. This further verifies that the lack of proton-capturing sites leads to blocked charge transfer caused by interfacial proton accumulation and severe retardation of reaction kinetics. Bode phase diagrams [Figure 7D-F] further clarify the kinetic characteristics of interfacial reactions. The phase angle peak of Ni_2Mo-$NiOOH/MoO_x$ shifts toward the high-frequency direction and continuously increases in intensity as the potential rises, implying a greatly shortened time constant of interfacial reactions and a markedly enhanced Faradaic reaction rate. The high-frequency shift of the phase angle peak directly reflects the acceleration effect of MoO_x proton-capturing sites on the PCET process. The Mo=O/Mo-O^- mediated rapid proton transfer effectively reduces the coupling resistance between charge transfer and proton transport, thereby lowering the kinetic time constant of UOR Faradaic reactions. Meanwhile, the continuous enhancement of peak intensity suggests that the Faradaic contribution of UOR increases gradually with elevated potential, enabling the catalyst to efficiently drive the reaction even at low applied potentials. On the contrary, the amplitude of the high-frequency shift of the phase angle peak for Ni_2

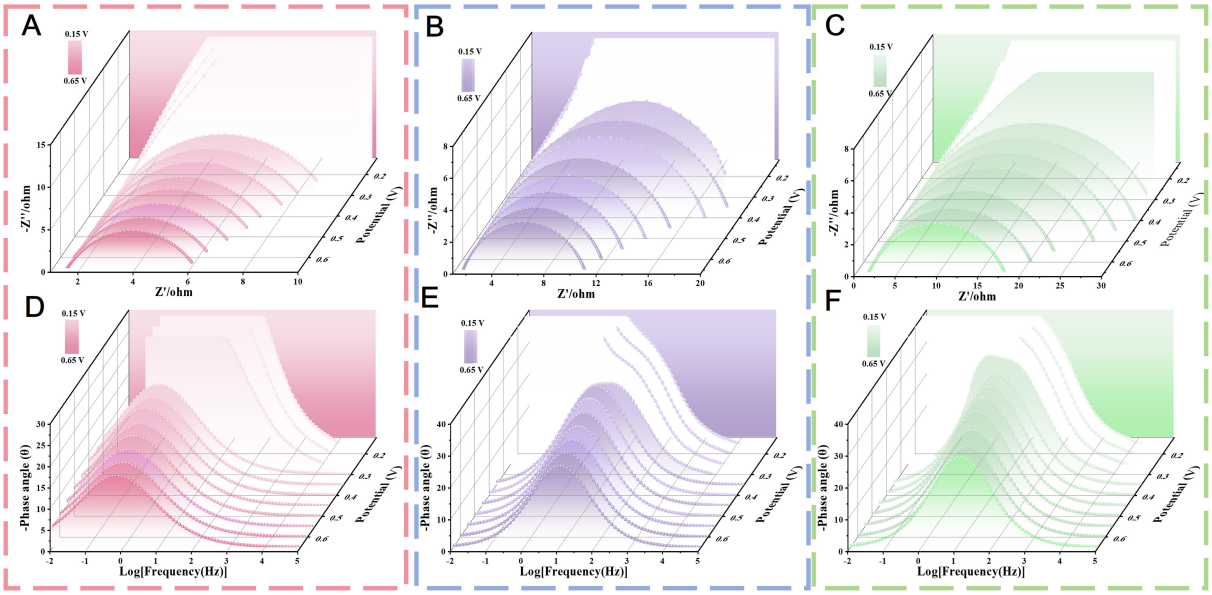

Figure 7. Operando EIS characterization of various catalytic electrodes (potential range: 0.15-0.65 V *vs.* SCE). (A-C) 3D waterfall plots of Nyquist impedance spectra; (D-F) 3D waterfall plots of Bode phase diagrams; (A and D) Ni_2Mo-NiOOH/MoO_x; (B and E) Ni_2Mo/NF; (C and F) Ni-NiOOH. EIS: Electrochemical impedance spectroscopy; SCE: saturated calomel electrode; NF: nickel foam.

Mo/NF is much smaller than that of Ni_2Mo-NiOOH/MoO_x, with a broadened peak shape and low intensity at low potentials, which reflects its limited interfacial proton transport efficiency and inadequate acceleration of the PCET process. The phase angle peak of Ni-NiOOH barely shifts within the entire potential range and maintains a consistently low intensity, further confirming that interfacial proton accumulation seriously retards reaction kinetics without the participation of proton-capturing sites.

In summary, the dynamic characterization results of *in situ* EIS three-dimensional waterfall plots fully reveal the pivotal regulatory role of MoO_x proton-capturing sites in Ni_2Mo-NiOOH/MoO_x. By rapidly capturing H^+ released during UOR dehydrogenation and constructing interfacial proton transfer pathways, these sites effectively mitigate interfacial polarization and proton accumulation, and synergistically optimize the kinetics of charge transfer and proton transport together with NiOOH active sites.

Purification performance of high-concentration urea wastewater

To evaluate the practical application potential of the Ni_2Mo-NiOOH/MoO_x electrocatalyst in urea-containing wastewater treatment and coupled urea oxidation systems, the diacetyl monoxime-antipyrine method (Chinese national standard method) was employed to measure the urea degradation efficiency[52]. The urea degradation performance of various catalysts was systematically investigated through ultraviolet–visible spectroscopy (UV-Vis) absorption spectroscopy, solution color variation and real-time monitoring of urea concentration [Figure 8].

As shown in Figure 8A, the characteristic absorption peak corresponding to urea degradation in the Ni_2Mo-NiOOH/MoO_x system decays rapidly with prolonged reaction time. After 420 min, the absorption intensity drops to only 2.79% of the initial value, corresponding to an ultrahigh urea removal efficiency of 97.21%. This value is remarkably superior to those of Ni_2Mo/NF (87.96%) [Figure 8D] and Ni-NiOOH (81.16%) [Figure 8G]. The solution color changes intuitively confirm such performance differences [Figure 8B, E and H]. The yellow color of the solution in the Ni_2Mo-NiOOH/MoO_x system fades rapidly as the reaction proceeds, while obvious color residue can still be observed in the control catalyst systems, directly reflecting

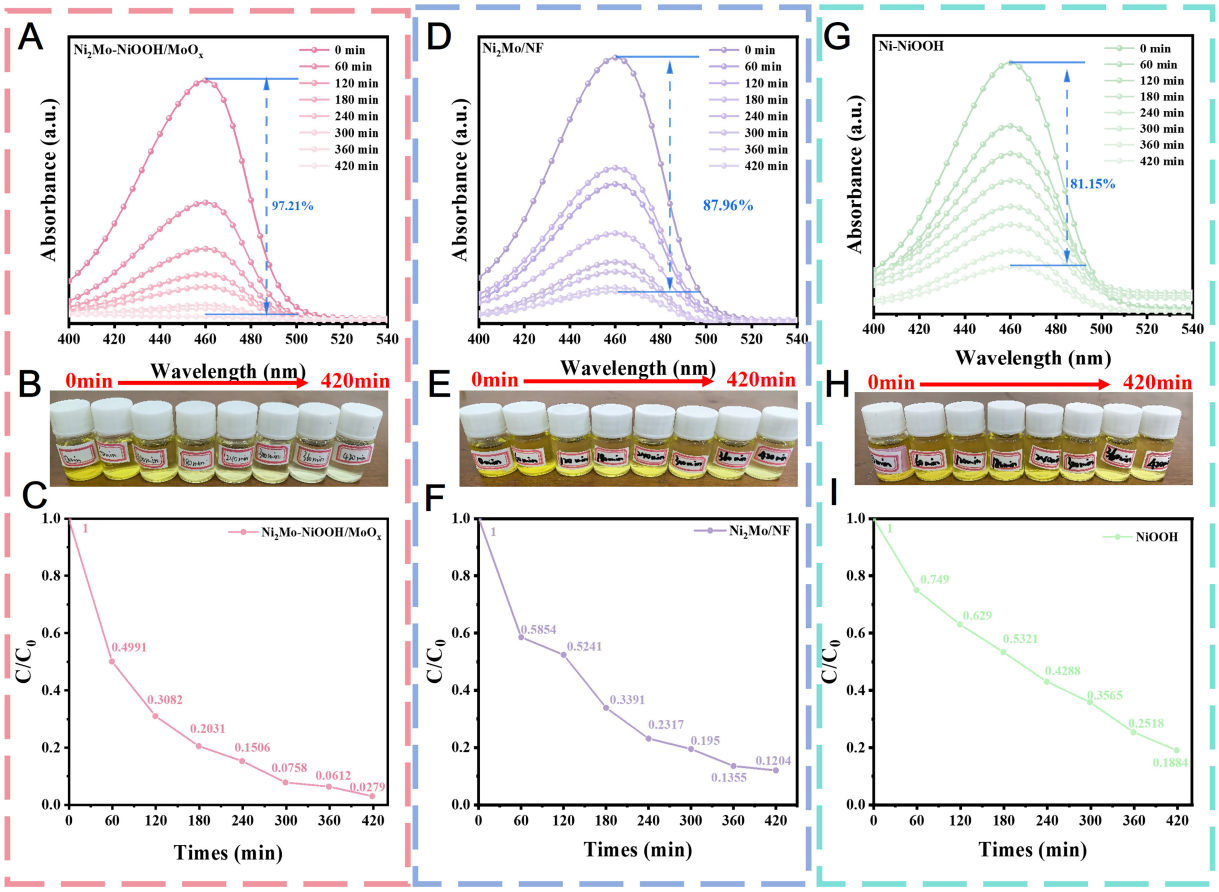

Figure 8. Urea degradation performance characterization of different catalytic electrodes. (A, D, G) UV-Vis absorption spectra at different reaction times; (B, E, H) Photographs of solution color evolution during the reaction; (C, F, I) Variation curves of relative urea concentration C/C_0 as a function of reaction time; where (A)-(C), (D)-(F), and (G)-(I) correspond to the test results of Ni_2Mo-NiOOH/MoO_x, Ni_2Mo/NF, and Ni-NiOOH catalysts, respectively. NF: Nickel foam.

Ni_2Mo-NiOOH/MoO_x system outstanding urea degradation capability. The time-dependent relative urea concentration curves [Figure 8C, F and I] further quantitatively reveal the kinetic differences. Ni_2Mo-NiOOH/MoO_x exhibits a much faster decline rate of urea concentration, with the C/C_0 value decreasing to 2.79% within 420 min. By contrast, the C/C_0 values of Ni_2Mo/NF and Ni-NiOOH remain as high as 12.04% and 18.84%, respectively, demonstrating the optimal urea conversion efficiency and reaction rate of Ni_2Mo-NiOOH/MoO_x. Such prominent superiority fundamentally originates from the synergistic regulation between NiOOH active sites and MoO_x proton-capturing sites. As the oxidative active center, NiOOH efficiently drives the adsorption and bond dissociation of urea molecules. Meanwhile, the *in situ* generated Mo=O/Mo-O^- species can rapidly trap H^+ released during the *-NH_2 dehydrogenation step, effectively alleviate interfacial proton accumulation, markedly lower the energy barrier of the key PCET step, and accelerate UOR kinetics, thus achieving efficient urea degradation under practical working conditions. In comparison, Ni_2Mo/NF fails to form stable and efficient MoO_x proton-capturing sites, resulting in insufficient interfacial proton dissipation and restricted reaction kinetics. Ni-NiOOH without MoO_x proton-capturing sites lacks the proton capture mechanism; the accumulated interfacial protons retard the UOR process and greatly reduce the urea degradation efficiency.

From the perspective of practical application, Ni_2Mo-NiOOH/MoO_x achieves nearly complete urea removal within 420 min, showing great application potential in urea-containing wastewater treatment, direct urea fuel cells, and urea-assisted hydrogen production coupling systems. This work provides a feasible practical

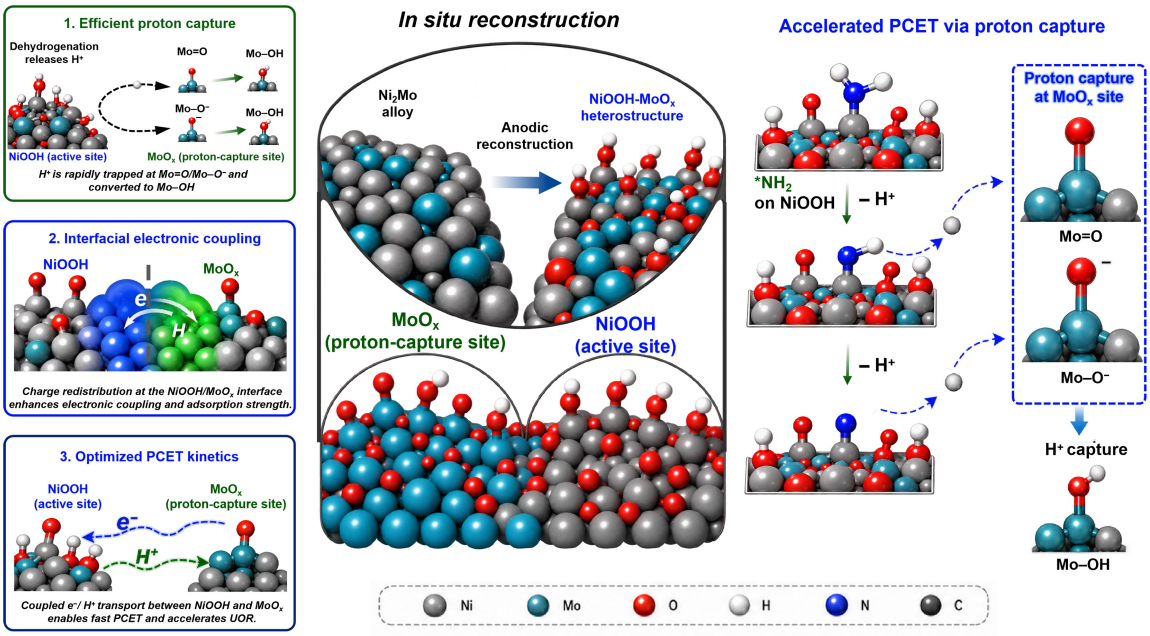

Figure 9. Schematic mechanism of the Ni_2Mo-NiOOH/MoO_x catalytic electrode during UOR. PCET: Proton-coupled electron transfer; UOR: urea oxidation reaction.

strategy for developing low-cost and high-activity electrocatalysts toward urea oxidation, and further verifies the reliability and superiority of this synergistic catalytic strategy under practical operating conditions.

Figure 9 illustrates the catalytic electrode with dynamically reconstructed Ni_2Mo-NiOOH/MoO_x, which possesses a heterogeneous interface co-constructed by NiOOH active phases and MoO_x species. The NiOOH phase functions as the core oxidative active center, providing reactive sites for the adsorption and stepwise dehydrogenation of urea molecules and driving the forward progression of UOR. Meanwhile, the synchronously generated MoO_x is rich in Mo=O/Mo-O^- species, which can act as efficient proton-capturing centers. These sites rapidly trap protons released from the *-NH_2 dehydrogenation step, effectively alleviate the polarization effect caused by interfacial proton accumulation, and markedly lower the reaction energy barrier of the key PCET step. Consequently, the synergistic regulation of oxidative catalysis and proton conduction is achieved, which substantially accelerates the reaction kinetics of UOR.

CONCLUSION

In summary, Ni_2Mo-NiOOH/MoO_x electrocatalyst was successfully fabricated via an anodic *in situ* reconstruction strategy, which exhibits outstanding UOR electrocatalytic activity and long-term structural stability. Benefiting from the significant enhancement of UOR catalytic activity induced by *in situ* reconstruction, the catalyst achieves a current density of 100 mA·cm^{-2} at only 1.341 V *vs.* RHE, which is merely 111 mV higher than the theoretical OER potential (1.23 V) and a small Tafel slope of 32.36 mV·dec^{-1}, demonstrating favorable reaction kinetics. Structural characterization and electrochemical measurements confirm that the anodic reconstruction process not only transforms the Ni_2Mo/NF into a Ni_2Mo-NiOOH/MoO_x composite structure, but also creates efficient proton-capturing sites rich in Mo=O/Mo-O^- species. These sites can rapidly trap H^+ released from the *-NH_2 dehydrogenation process during UOR, effectively alleviate interfacial proton accumulation, and greatly lower the energy barrier of the key PCET step. Meanwhile, the Mo-induced local charge rearrangement further optimizes the adsorption/desorption energy barrier of UOR intermediates and improves the intrinsic catalytic activity of Ni active sites. *In situ* Raman spectroscopy, *in situ* EIS and electrolyte control experiments further verify that the *in situ* generated

MoO_x proton-capturing sites act as the core motive for accelerating reaction kinetics. The reversible proton transfer cycle of MoO_x species synergizes with NiOOH active sites to construct efficient electron/proton synergistic transfer pathways for the UOR process. Attributed to the above superior performances, Ni_2Mo-NiOOH/MoO_x achieves a urea degradation efficiency of 97.21% within 420 min, and maintains a high current retention of 98.75% after continuous operation for 300 h at 100 $mA·cm^{-2}$. It presents broad practical application prospects in the fields of urea electrolysis for hydrogen production and collaborative treatment of urea-containing wastewater. Furthermore, the proposed strategy of *in situ* reconstruction-mediated synergistic regulation of active sites and proton-capturing sites provides a novel design philosophy and universal reference for the development of high-efficiency UOR electrocatalysts.

DECLARATIONS

Authors' contributions

Writing-original draft, methodology, investigation, formal analysis, data curation: Liu, J.
Writing-review & editing: Zhou, M.
Visualization, investigation: Wang, C.
Project administration: Zhou, L.
Conceptualization: Ruan, M.
Writing-review & editing, supervision, funding acquisition: Liu, Z.

Availability of data and materials

The original contributions presented in this study are included in the article/Supplementary Materials. Further inquiries can be directed to the corresponding authors.

AI and AI-assisted tools statement

During the preparation of this manuscript, the AI tool WPS AI (WPS AI 1.0, algorithm filing identifier: Beijing-WPS-AI, dated 2023-10-16) was used for visual processing and graphical optimization of Figure 9 and the Graphical Abstract. Specifically, in Figure 9, WPS AI was used to segment/cut out the molecular structures, followed by their integration, layout adjustment, annotation, and final graphical optimization using WPS and WPS AI. In the Graphical Abstract, WPS AI was used to cut out and enhance the scanning electron microscopy (SEM) image of the sample acquired by the authors, followed by integration, layout adjustment, annotation, and final graphical optimization using WPS and WPS AI. The tool did not influence the study design, data collection, analysis, interpretation, or the scientific content of the work. All authors take full responsibility for the accuracy, integrity, and final content of the manuscript.

Financial support and sponsorship

The authors gratefully acknowledge the support from the National Natural the Science Foundation of China (No. 52373301, No. 22678414 and No. 22508289), the Science Foundation of Tianjin (No. 23JCZDJC00180 and No. 25JCQNJC00260), and the Joint Research Center of China and Foreign Countries Special Fund of Tianjin Innovation Platform (No. 24PTLYHZ00240).

Conflicts of interest

All authors declared that there are no conflicts of interest.

Ethical approval and consent to participate

Not applicable.

Consent for publication

Not applicable.

Copyright

© The Author(s) 2026.

Supplementary Materials

Supplementary Materials

REFERENCES

1. Kempler, P. A.; Coridan, R. H.; Luo, L. Gas evolution in water electrolysis. *Chem. Rev.* **2024**, *124*, 10964-1007. DOI PubMed
2. Zhang, W.; Liu, M.; Gu, X.; Shi, Y.; Deng, Z.; Cai, N. Water electrolysis toward elevated temperature: advances, challenges and frontiers. *Chem. Rev.* **2023**, *123*, 7119-92. DOI PubMed
3. Yu, L.; Ning, M.; Wang, Y.; Yuan, C.; Ren, Z. Direct seawater electrolysis for hydrogen production. *Nat. Rev. Mater.* **2025**, *10*, 857-73. DOI
4. Esfandiari, N.; Aliofkhazraei, M.; Colli, A. N.; et al. Metal-based cathodes for hydrogen production by alkaline water electrolysis: review of materials, degradation mechanism, and durability tests. *Prog. Mater. Sci.* **2024**, *144*, 101254. DOI
5. dos Santos, K. G.; Eckert, C. T.; De Rossi, E.; et al. Hydrogen production in the electrolysis of water in Brazil, a review. *Renew. Sustain. Energy Rev.* **2017**, *68*, 563-71. DOI
6. Yang, J.; Lam, T. Y.; Luo, Z.; Cheng, Q.; Wang, G.; Yao, H. Renewable energy driven electrolysis of water for hydrogen production, storage, and transportation. *Renew. Sustain. Energy Rev.* **2025**, *218*, 115804. DOI
7. Yu, J.; Li, Z.; Wang, C.; et al. Engineering advanced noble-metal-free electrocatalysts for energy-saving hydrogen production from alkaline water via urea electrolysis. *J. Colloid Interface Sci.* **2024**, *661*, 629-61. DOI
8. Zhang, L.; Wang, L.; Lin, H.; et al. A lattice-oxygen-involved reaction pathway to boost urea oxidation. *Angew. Chem.* **2019**, *131*, 16976-81. DOI
9. Kong, Z.; Wu, J.; Liu, Z.; Yan, D.; Wu, Z. P.; Zhong, C. J. Advanced electrocatalysts for fuel cells: evolution of active sites and synergistic properties of catalysts and carrier materials. *Exploration* **2024**, *5*, 20230052. DOI PubMed PMC
10. Zemtsova, V. M.; Oshchepkov, A. G.; Savinova, E. R. Unveiling the role of iron in the nickel-catalyzed urea oxidation reaction. *ACS Catal.* **2023**, *13*, 13466-73. DOI
11. Rasal, A. S.; Chen, H. M.; Yu, W. Electronic structure engineering of electrocatalyst for efficient urea oxidation reaction. *Nano Energy* **2024**, *121*, 109183. DOI
12. Wang, L.; Zhu, Y.; Wen, Y.; et al. Regulating the local charge distribution of Ni active sites for the urea oxidation reaction. *Angew. Chem. Int. Ed. Engl.* **2021**, *60*, 10577-82. DOI PubMed
13. Lee, J. W.; Lee, D.; Lee, H.; Shim, S.; Kim, J. H.; Lee, C. Enhanced oxidation of urea by pH swing during chlorination: pH-dependent reaction mechanism. *Water Res.* **2023**, *242*, 120183. DOI
14. Zhou, L.; Feng, D.; Liu, C.; Sun, Y.; Fu, Y.; Ma, T. Amorphous $Ni(OH)_2$-Ni_3S_2/NF nano-flower heterostructure catalyst promotes efficient urea assisted overall water splitting. *Chem. Asian J.* **2024**, *19*, e202300980. DOI PubMed
15. Li, M.; Wu, X.; Liu, K.; et al. Nitrogen vacancies enriched Ce-doped Ni_3N hierarchical nanosheets triggering highly-efficient urea oxidation reaction in urea-assisted energy-saving electrolysis. *J. Energy Chem.* **2022**, *69*, 506-15. DOI
16. Zhang, J.; Song, X.; Kang, L.; et al. Stabilizing efficient structures of superwetting electrocatalysts for enhanced urea oxidation reactions. *Chem. Catal.* **2022**, *2*, 3254-70. DOI
17. Zeng, F.; Mebrahtu, C.; Liao, L.; Beine, A. K.; Palkovits, R. Stability and deactivation of OER electrocatalysts: a review. *J. Energy Chem.* **2022**, *69*, 301-29. DOI
18. Zheng, Z.; Wu, D.; Chen, L.; et al. Collaborative optimization of thermodynamic and kinetic for Ni-based hydroxides in electrocatalytic urea oxidation reaction. *Appl. Catal. B Environ.* **2024**, *340*, 123214. DOI
19. Liu, Q.; Zhao, F.; Yang, X.; et al. Constructing interlaced network structure by grain boundary corrosion methods on CrCoNiFe alloy for high-performance oxygen evolution reaction and urea oxidation reaction. *J. Mater. Sci. Technol.* **2024**, *203*, 97-107. DOI
20. Xu, S.; Jiao, D.; Ruan, X.; et al. O-2p hybridization enhanced transformation of active γ-NiOOH by chromium doping for efficient urea oxidation reaction. *Adv. Funct. Mater.* **2024**, *34*, 2401265. DOI
21. Wang, Y.; Qian, G.; Xie, Z.; et al. Strengthening CuNiCoMo medium-entropy alloy by tuning local lattice tensile strain and built-in electric field for boosting urea oxidation reaction. *Appl. Catal. B: Environ. Energy* **2025**, *365*, 124841. DOI
22. Du, M.; Ji, Y.; Li, Y.; (Frank) Liu, S.; Yan, J. Construction of an internal charge field: $CoS_{1.097}$/Ni_3S_2 heterojunction promotes efficient urea oxidation reaction. *Adv. Funct. Mater.* **2024**, *34*, 2402776. DOI
23. Ni, S.; Qu, H.; Xu, Z.; et al. Interfacial engineering of the $NiSe_2$/$FeSe_2$ p-p heterojunction for promoting oxygen evolution reaction and electrocatalytic urea oxidation. *Appl. Catal. B Environ.* **2021**, *299*, 120638. DOI
24. Wang, P.; Zheng, W.; Qu, Y.; et al. Photo-excited high-spin state Ni (III) species in Mo-doped Ni_3S_2 for efficient urea oxidation reaction. *Small* **2024**, *20*, 2403107. DOI PubMed
25. Xu, S.; Ruan, X.; Ganesan, M.; Wu, J.; Ravi, S. K.; Cui, X. Transition metal-based catalysts for urea oxidation reaction (UOR): catalyst design strategies, applications, and future perspectives. *Adv. Funct. Mater.* **2024**, *34*, 2313309. DOI

26. Zhong, M.; Xu, M.; Ren, S.; et al. Modulating the electronic structure of $Ni(OH)_2$ by coupling with low-content Pt for boosting the urea oxidation reaction enables significantly promoted energy-saving hydrogen production. *Energy Environ. Sci.* **2024**, *17*, 1984-96. DOI
27. Zhang, S.; Jin, M.; Xu, H.; et al. An oxygen-coordinated cobalt single-atom electrocatalyst boosting urea and urea peroxide production. *Energy Environ. Sci.* **2024**, *17*, 1950-60. DOI
28. Gao, X.; Zhang, S.; Wang, P.; Jaroniec, M.; Zheng, Y.; Qiao, S. Z. Urea catalytic oxidation for energy and environmental applications. *Chem. Soc. Rev.* **2024**, *53*, 1552-91. DOI
29. Geng, S. K.; Zheng, Y.; Li, S. Q.; et al. Nickel ferrocyanide as a high-performance urea oxidation electrocatalyst. *Nat. Energy* **2021**, *6*, 904-12. DOI
30. Zhang, J.; Zhu, J.; Kang, L.; et al. Balancing dynamic evolution of active sites for urea oxidation in practical scenarios. *Energy Environ. Sci.* **2023**, *16*, 6015-25. DOI
31. Yang, C.; Pang, H.; Li, X.; et al. Scalable electrocatalytic urea wastewater treatment coupled with hydrogen production by regulating adsorption behavior of urea molecule. *Nanomicro Lett.* **2025**, *17*, 159. DOI PubMed PMC
32. Zheng, X.; Yang, J.; Li, P.; et al. Dual-atom support boosts nickel-catalyzed urea electrooxidation. *Angew. Chem.* **2023**, *135*, e202217449. DOI
33. Liu, J.; Chen, Y.; Zhou, M.; Liu, Z. Synergistic Al-induced stabilization of Fe-O bonds to mitigate Fe^{3+} leaching and oxygen vacancy for enhanced urea oxidation catalysis. *Chem. Eng. J.* **2026**, *531*, 173953. DOI
34. Lu, S.; Zheng, X.; Wang, H.; et al. Energy-saving hydrogen production by heteroatom modulations coupling urea electrooxidation. *EcoMat* **2024**, *6*, e12477. DOI
35. Gao, X.; Bai, X.; Wang, P.; et al. Boosting urea electrooxidation on oxyanion-engineered nickel sites via inhibited water oxidation. *Nat. Commun.* **2023**, *14*, 5842. DOI PubMed PMC
36. Jiang, W.; Zhang, J.; Wu, J.; et al. Regulating the competitive adsorption of urea and OH^- via brønsted base intercalated nickel sites for highly selective urea oxidation. *Adv. Energy Mater.* **2026**, *16*, e03978. DOI
37. Yang, J.; Wang, Y.; Fan, Y.; Xu, B.; Tu, T. Sustainable recycling of polyamides via C-N bond cleavage facilitated by methyl tosylate under mild conditions. *Nat. Commun.* **2025**, *16*, 8884. DOI PubMed PMC
38. Ni, X.; Luo, Z.; Sun, H.; et al. Multi-site relay catalysis for efficient hydrogen production coupled with urea-rich wastewater treatment at large current density. *Appl. Catal. B: Environ. Energy* **2026**, *399*, 127132. DOI
39. Ma, Z.; Liu, X.; Wang, H.; et al. Interfacial engineering of NiCo nanocones to promote NiOOH formation via enhanced dehydrogenation for efficient urea electrooxidation. *Adv. Energy Mater.* **2026**, *16*, e02563. DOI
40. Chen, W.; Xu, L.; Zhu, X.; et al. Unveiling the electrooxidation of urea: intramolecular coupling of the N-N bond. *Angew. Chem. Int. Ed. Engl.* **2021**, *60*, 7297-307. DOI PubMed
41. Sari, F. N. I.; Tran, N. T. T.; Ke, M.; Purba, Y.; Huynh, T. M. D.; Ting, J. M. Suppression of oxygen electrooxidation toward enhanced urea electrooxidation via balancing the adsorption of OH- and urea intermediates in quaternary-metal LDH. *Chem. Eng. J.* **2025**, *515*, 163966. DOI
42. Wang, J.; Sun, M.; Zhang, X.; et al. pH-dependent urea electrooxidation: from mechanism to catalysts and applications. *Adv. Mater.* **2026**, *38*, e15043. DOI PubMed
43. Gong, Z.; Xu, M.; Li, P.; Ye, G.; Li, W.; Fei, H. Rapid reconstruction of amorphous/crystalline heterojunction boosts nickel-catalyzed urea electrooxidation. *ACS Catal.* **2025**, *15*, 20958-67. DOI
44. Yang, H.; Li, T.; Li, Z.; Huang, K.; Zhang, Z.; Meng, X. Dual-metal regulation of PCET and spin polarization synergism for efficient photocatalytic urea synthesis. *Chem. Eng. J.* **2025**, *522*, 167328. DOI
45. Derosa, J.; Garrido-Barros, P.; Li, M.; Peters, J. C. Use of a PCET mediator enables a Ni-HER electrocatalyst to act as a hydride delivery agent. *J. Am. Chem. Soc.* **2022**, *144*, 20118-25. DOI PubMed
46. Hou, L.; Sun, C.; Zhang, Z.; et al. Carbon-oxyanion atomically steering direct urea oxidation on NiOOH at industrial current densities. *Adv. Funct. Mater.* **2025**, *36*, e19865. DOI
47. Wang, P.; Gao, X.; Zheng, M.; Jaroniec, M.; Zheng, Y.; Qiao, S. Z. Urine electrooxidation for energy-saving hydrogen generation. *Nat. Commun.* **2025**, *16*, 2424. DOI PubMed PMC
48. Yu, X.; Zhang, W.; Ma, L.; et al. Interfacial engineering of a CoSe@NiFe heterostructure electrocatalyst for high-efficiency water and urea oxidation. *Green Chem.* **2025**, *27*, 731-42. DOI
49. Zeng, M.; Wu, J.; Li, Z.; et al. Interlayer effect in NiCo layered double hydroxide for promoted electrocatalytic urea oxidation. *ACS Sustainable Chem. Eng.* **2019**, *7*, 4777-83. DOI
50. Liu, J.; Zhou, M.; Chen, Y.; Liang, X.; Liu, Z. Etching reconstruction of ultrathin layered NiFe-hydroxide: building synergistic $V_{Fe(III)}$/Ni(III) active structures for an efficient urea oxidation reaction. *Green Chem.* **2026**, *28*, 11533-47. DOI

51. Wang, L.; Zhao, Z. Dynamic adsorption of molybdate promoted self-optimization and self-healing of NiFe/NiMo in alkaline water electrolysis. *Small* **2026**, *22*, e10965. DOI PubMed

52. Qiao, P.; Li, G.; Xu, X.; et al. Mediating self-oxidation and competitive adsorption for achieving high-selective urea oxidation catalysis at industrial-level current densities. *Adv. Funct. Mater.* **2025**, *35*, 2421136. DOI

Disclaimer/Publisher's Note: All statements, opinions, and data contained in this publication are solely those of the individual author(s) and contributor(s) and do not necessarily reflect those of OAE and/or the editor(s). OAE and/or the editor(s) disclaim any responsibility for harm to persons or property resulting from the use of any ideas, methods, instructions, or products mentioned in the content.

© The Author(s) 2026. Open Access This article is licensed under a Creative Commons Attribution 4.0 International License (https://creativecommons.org/licenses/by/4.0/), which permits unrestricted use, sharing, adaptation, distribution and reproduction in any medium or format, for any purpose, even commercially, as long as you give appropriate credit to the original author(s) and the source, provide a link to the Creative Commons license, and indicate if changes were made.